

The Spectral Signature of Dust Scattering and Polarization in the Near IR to Far UV. I. Optical Depth and Geometry Effects

Victor G. Zubko¹ and Ari Laor

Department of Physics, Technion – Israel Institute of Technology, Haifa 32000, Israel

ABSTRACT

Spectropolarimetry from the near IR to the far UV of light scattered by dust provides a valuable diagnostic of the dust composition, grain size distribution and spatial distribution. To facilitate the use of this diagnostic, we present detailed calculations of the intensity and polarization spectral signature of light scattered by optically thin and optically thick dust in various geometries. The polarized light radiative transfer calculations are carried out using the adding-doubling method for a plane-parallel slab, and are extended to an optically thick sphere by integrating over its surface. The calculations are for the Mathis, Rumpel & Nordsieck Galactic dust model, and cover the range from 1 μm to 500 \AA .

We find that the wavelength dependence of the scattered light intensity provides a sensitive probe of the optical depth of the scattering medium, while the polarization wavelength dependence provides a probe of the grain scattering properties, which is practically independent of optical depth. We provide a detailed set of predictions, including polarization maps, which can be used to probe the properties of dust through imaging spectropolarimetry in the near IR to far UV of various Galactic and extragalactic objects. In a following paper we use the codes developed here to provide predictions for the dependence of the intensity and polarization on grain size distribution and composition.

Subject headings: dust, extinction — radiative transfer — scattering — polarization — ISM: globules — methods: numerical

1. Introduction

Light scattering induces polarization, and the intensity and polarization of the scattered light tells us the properties of the scattering medium. Continuum radiation can be scattered over large volumes of space either by free electrons, or by dust grains in either diffuse or compact clouds. Electron scattering is wavelength independent (below X-ray energies) and follows a simple scattering phase function ($\propto 1 + \cos^2 \Theta_{\text{scat}}$), but dust scattering is much more complicated since the scattering efficiency and the phase function can be strongly dependent on wavelength, grain size, and grain composition. Thus, light scattered by dust carries valuable information on the dust properties, and the purpose of this paper is to facilitate the extraction of this information.

Dust reflected light is observed in various Galactic objects, either from large and diffuse reflection nebulae (e.g. Witt et al. 1992, 1993; Gordon et al. 1994; Calzetti et al. 1995), or from more compact, but still spatially resolved objects, such as dense molecular clumps (e.g. the Eagle nebula, Hester et al. 1996),

¹On leave from the Main Astronomical Observatory, National Academy of Sciences of the Ukraine, Kiev

protoplanetary disks (the Orion nebula, O’Dell, Wen, & Hu 1993; Bally et al. 1998), cometary knots in planetary nebulae (Balick et al. 1998; Burkert & O’Dell 1998), and bipolar nebulae (the Egg nebula, Sahai et al. 1998a,b). Dust reflection is also inferred in some compact unresolved objects (e.g. Schulte-Ladbeck et al. 1992; Rees & Sitko 1996), and is also likely to be present in young stellar objects with circumstellar disks (e.g. Chiang & Goldreich 1997).

Dust reflected light is also observed in various extragalactic objects. In particular in active galaxies, where dust obscuration plays a key role in unification schemes (Antonucci 1993; Urry & Padovani 1995). Specific evidence for scattering is present in Seyfert 2 galaxies (e.g. Antonucci & Miller 1985; Miller, Goodrich & Mathews 1995; Tran 1995a,b; Capetti et al. 1996), radio galaxies (e.g. Jannuzi et al. 1995; Dey et al. 1996; Cimatti et al. 1998; Tran et al. 1998; Hurt et al. 1999), broad absorption line quasars (e.g. Cohen et al. 1995; Goodrich & Miller 1995; Schmidt & Hines et al. 1999), red quasars (e.g. Brotherton et al. 1998; De Breuck et al. 1998), and ultraluminous IR active galaxies (e.g. Wills et al. 1992; Hines & Wills 1993; Hines et al. 1999). In some of these objects the polarization rises towards shorter wavelengths, strongly suggesting optically thin dust scattering.

Despite its potential usefulness, almost no data currently exists on spectropolarimetry of spatially resolved scattered light in Galactic objects (see a rare exception in Code et al. 1996). Fortunately, significant amounts of spectropolarimetry, though mostly spatially unresolved, are available for extragalactic objects, in particular at the rest frame UV (for high z objects), where most of the spectral polarization features are predicted, and which therefore provides the strongest diagnostic power.

In this paper we provide a detailed set of predictions for the wavelength dependence of the intensity, percent polarization, polarization plane, and circular polarization, of light scattered by dust in the near IR to the far UV. These properties are explored here for a given dust model over a range of scattering geometries for either optically thin or optically thick dust. In a following paper we explore these properties for various dust models, as characterized by the grain size distribution and grain composition. These predictions, together with new high quality spectropolarimetry in the near IR to the far UV of reflection dominated objects, should allow significant constraints on the properties of dust in various Galactic and extragalactic environments.

Earlier calculations of polarized radiative transfer in a dusty optically thick medium were made by White (1979a,b), Kartje (1995), Code & Whitney (1995), and Wolf & Henning (1999; see also optically thin calculations for radio galaxies in Manzini & di Serego Alighieri 1996). The calculations presented here improve on these earlier calculations either by the use of an accurate radiative transfer, rather than a Monte Carlo calculation, or by using updated dielectric functions of silicate and graphite grains, by using the actual, rather than approximated scattering phase matrix, by extending our results down to 500 Å (relevant for high redshift extra galactic objects), and by the detailed set of results presented.

The paper is organized as follows. In §2 we provide a detailed description of the theoretical approach. The results for scattering by optically thin dust, and by an optically thick slab and sphere are presented in §3, and the paper is summarized in §4. A detailed description of the numerical implementation is provided in the Appendix, where we also provide tests of the codes based on a comparison with accurate analytic results for electron scattering, and with earlier numerical results for dust scattering. We also show in the Appendix a comparison with the much simpler case of an electron scattering sphere.

2. Theoretical approach

The main purpose of this paper is to study in detail the wavelength dependence of scattering and polarization of light incident on optically thick dust in simple geometrical configurations. The distance from the illumination source to the dusty nebula is assumed here to be much larger than the characteristic length corresponding to an optical depth $\tau \sim 1$ within the dusty nebula, so one may use the parallel illumination assumption. Dusty slabs or spheres are the simplest possible dust configurations to consider, and are relevant for the various optically thick scattering objects mentioned in §1.

Radiative transfer in a plane-parallel slab is a standard problem in the theory of radiative transfer (Chandrasekhar 1960). To solve this problem we use the adding-doubling method (Hovenier 1971; Hansen & Travis 1974; Evans & Stephens 1991), which is efficient and numerically stable up to large optical depths. We follow the formulation of the adding-doubling method proposed by Evans & Stephens (1991). To solve the case of an optically thick dusty sphere, we assume that the geometrical depth at which $\tau \sim 1$ is much smaller than the radius of the sphere, so the surface of the sphere can be treated as a collection of a large number of small plane-parallel slabs with a horizontal size much less than the sphere radius, but still much larger than the vertical depth at which $\tau \sim 1$. The scattering properties of the sphere are obtained by integrating the local solution for the slabs over the sphere surface. Note that the surface integration approach can be applied to practically any optically thick geometry.

Light scattering by a sphere can also be calculated using the Monte Carlo method (Witt 1977), as was done by Code & Whitney (1995). However, the efficiency of the Monte Carlo method drops steeply at large optical depths, typically for $\tau > 5$ –10 (Fischer, Henning, & Yorke 1994; Code & Whitney 1995; Wolf & Henning 1999), and it does not allow the accuracy provided by an exact numerical radiative transfer for a large optical depth. However, the disadvantage of the numerical scheme employed here for a sphere is that it applies only for $\tau \gg 1$, unlike the Monte Carlo method which allows one to treat spheres with intermediate optical depth.

In the following subsections we provide a detailed description of our theoretical approach. We first briefly review the basics of single scattering by ensembles of spherical grains (section 2.1), introducing the phase matrix, albedo, and other parameters relevant for multiple scattering. In section 2.2 we describe the polarized radiative transfer in a slab, which provides the basis for this and forthcoming studies. In section 2.2.1 we formulate the problem and introduce the main parameters. We next derive the expression for the scattering matrix (section 2.2.2) in a form suitable for efficient implementation of the adding-doubling method, which is described in section 2.2.3. In section 2.3, we describe how to calculate the scattering characteristics of an optically thick sphere using the solution for a slab.

2.1. Single scattering by dust grains

In order to solve the radiative transfer in an extended dusty medium, it is necessary to obtain first the scattering properties per unit volume. If the mean distance between dust particles in the medium considerably exceeds the typical grain size, and the particles are randomly distributed (as applies for cosmic dust), then there are no coherence effects and the particles scatter the light independently. The scattering also does not change the frequency. The transfer in larger, optically thick volumes, is studied by solving the equations of radiative transfer, using the results for the single scattering problem. In this section we introduce the main parameters which describe single scattering; the intensity vector, the phase matrix and the single-scattering albedo. We next present specific expressions of these parameters for the cases of Mie

and Rayleigh scattering relevant for the present study.

The intensity and polarization of a beam of light are fully described by the 4-vector \mathbf{I} of Stokes parameters (I, Q, U, V) (Chandrasekhar 1960; Bohren & Huffman 1983), defined with respect to a certain plane of reference. The parameter I describes the total light intensity, Q and U describe the linear polarization, frequently expressed through the degree of linear polarization $p_l = \sqrt{Q^2 + U^2}/I$ and the position angle of the direction of linear polarization with respect to the local meridian plane $\theta_p = \frac{1}{2} \arctan(U/Q)$, such that $\cos 2\theta_p$ has the same sign as Q . The last parameter, V , describes the circular polarization, and the degree of circular polarization is $p_c = V/I$. Note that the intensity vector \mathbf{I} is actually a *pseudo-vector*, since it does not transform like a true vector under a coordinate transformation. It is possible to build the so-called radiation density matrix $\hat{\rho}$ in terms of the Stokes parameters (Dolginov, Gnedin, & Silant'ev 1995)

$$\hat{\rho} = \frac{1}{2} \begin{bmatrix} I + Q & U + iV \\ U - iV & I - Q \end{bmatrix}, \quad (1)$$

which is a *tensor* in coordinate space. However, we base our calculations on the the intensity vector \mathbf{I} , as is common for cosmic dust studies.

The scattering from a small volume is obtained by summing over the scatterings of the grains within that volume. We assume a model of spherical grains, which is frequently used in various applications. The approach we develop is applicable not only for classical homogeneous spherical grains (Mie particles), but also for spherical grains of multilayer or composite structure.

If a grain of radius a is illuminated by parallel radiation of intensity \mathbf{I}_{in} at a wavelength λ , then the intensity of the radiation scattered by the grain in the direction Θ_{scat} and measured at a distance r in the far-field ($r \gg \lambda$) is

$$\mathbf{I}_{\text{out}}(\Theta_{\text{scat}}, a, \lambda) = \frac{\sigma_{\text{sca}}(a, \lambda)}{4\pi r^2} \mathcal{P}(\Theta_{\text{scat}}, a, \lambda) \mathbf{I}_{\text{in}} \quad (2)$$

where $\sigma_{\text{sca}}(a, \lambda)$ is the scattering cross-section of the grain and $\mathcal{P}(\Theta_{\text{scat}}, a, \lambda)$ is a 4-by-4 matrix called the phase matrix.

Since energy can be removed from the incident radiation by scattering as well as by absorption, it is important to introduce also the absorption and extinction cross-sections: σ_{abs} and $\sigma_{\text{ext}} = \sigma_{\text{sca}} + \sigma_{\text{abs}}$, respectively. Then we may define the so-called single-scattering albedo $\tilde{\omega} = \sigma_{\text{sca}}/\sigma_{\text{ext}}$, which gives the probability that a photon hitting a grain will be scattered. It is common to use the dimensionless efficiency factors for scattering, absorption and extinction, defined as ratios of respective cross-sections to the grain geometrical cross-section, equal in our specific case to πa^2 :

$$Q_{\text{sca}} = \frac{\sigma_{\text{sca}}}{\pi a^2}, \quad Q_{\text{abs}} = \frac{\sigma_{\text{abs}}}{\pi a^2}, \quad Q_{\text{ext}} = \frac{\sigma_{\text{ext}}}{\pi a^2}, \quad (3)$$

and thus $\tilde{\omega} = Q_{\text{sca}}/Q_{\text{ext}}$.

The phase matrix \mathcal{P} contains the full information about the angular distribution and state of polarization of the scattered radiation. For spherical grains, \mathcal{P} has an especially simple expression (Van de Hulst 1957; Bohren & Huffman 1983)

$$\mathcal{P}(\Theta_{\text{scat}}, a, \lambda) = \begin{bmatrix} P_1(\Theta_{\text{scat}}, a, \lambda) & P_2(\Theta_{\text{scat}}, a, \lambda) & 0 & 0 \\ P_2(\Theta_{\text{scat}}, a, \lambda) & P_1(\Theta_{\text{scat}}, a, \lambda) & 0 & 0 \\ 0 & 0 & P_3(\Theta_{\text{scat}}, a, \lambda) & P_4(\Theta_{\text{scat}}, a, \lambda) \\ 0 & 0 & -P_4(\Theta_{\text{scat}}, a, \lambda) & P_3(\Theta_{\text{scat}}, a, \lambda) \end{bmatrix}, \quad (4)$$

where only three of the four matrix elements are independent since: $P_1^2 = P_2^2 + P_3^2 + P_4^2$. The scattering plane, defined by the incoming and outgoing beams of light, is the plane of reference for the vectors of the Stokes parameters. The element P_1 is the phase function, which describes the probability that the unpolarized incident light will be scattered in any specific direction. The phase matrix \mathcal{P} is therefore normalized such that

$$\int_{4\pi} P_1 \frac{d\Omega}{4\pi} = 1. \quad (5)$$

The angular dependence of the phase function P_1 can be characterized by the so-called asymmetry parameter g :

$$g = \langle \cos \theta \rangle = \int_{4\pi} \cos \theta P_1 \frac{d\Omega}{4\pi}, \quad (6)$$

where g ranges from -1 (complete backscattering) to 1 (complete forward scattering) with $g = 0$ corresponding to isotropic scattering.

2.1.1. Mie scattering

Light scattering by a spherical homogeneous particle of an arbitrary radius a is given by the Mie series solution (the formulae presented here are valid also for the case of a concentric multilayer sphere). The elements of the phase matrix for a Mie-scattering particle are (Bohren & Huffman 1983):

$$\begin{aligned} P_1 &= \frac{2}{x^2 Q_{\text{sca}}} (|S_2|^2 + |S_1|^2), & P_2 &= \frac{2}{x^2 Q_{\text{sca}}} (|S_2|^2 - |S_1|^2), \\ P_3 &= \frac{2}{x^2 Q_{\text{sca}}} (S_2^* S_1 + S_2 S_1^*), & P_4 &= \frac{2i}{x^2 Q_{\text{sca}}} (S_2^* S_1 - S_2 S_1^*), \end{aligned} \quad (7)$$

where $x = 2\pi a/\lambda$ is the size parameter, and S_1 and S_2 are the scattering amplitudes, in general complex functions, for which the Mie theory gives (Bohren & Huffman 1983):

$$S_1(\mu) = \sum_{k=1}^{\infty} \frac{2k+1}{k(k+1)} [a_k \pi_k(\mu) + b_k \tau_k(\mu)], \quad S_2(\mu) = \sum_{k=1}^{\infty} \frac{2k+1}{k(k+1)} [a_k \tau_k(\mu) + b_k \pi_k(\mu)]. \quad (8)$$

where $\mu = \cos \Theta_{\text{scat}}$, the functions $\pi_k(\mu)$ and $\tau_k(\mu)$ contain the information about angular dependence, and a_k and b_k are the so-called scattering coefficients. The angular functions $\pi_k(\mu)$ and $\tau_k(\mu)$ can be calculated from the simple recursion relations (Bohren & Huffman 1983):

$$\pi_{k+2} = \frac{2k+3}{k+1} \mu \pi_{k+1} - \frac{k+2}{k+1} \pi_k, \quad \tau_{k+2} = (k+2) \mu \tau_{k+1} - (k+3) \tau_k, \quad (9)$$

starting from $\pi_0=0$ and $\pi_1=1$. The coefficients a_k and b_k , which are generally complex, characterize the contribution of various multipole modes to the scattering process. These are dependent on a , λ and the grain material complex refractive index $n = n_r + in_i$. The specific expressions for a_k and b_k , which are also calculated with recursion relations, may be found, e.g. in Bohren & Huffman (1983).

Once a_k and b_k are known, the efficiency factors Q_{sca} and Q_{ext} , and the asymmetry parameter g , are given by (Bohren & Huffman 1983):

$$Q_{\text{sca}} = \frac{2}{x^2} \sum_{k=1}^{\infty} (2k+1) (|a_k|^2 + |b_k|^2), \quad Q_{\text{ext}} = \frac{2}{x^2} \sum_{k=1}^{\infty} (2k+1) \Re\{a_k + b_k\}, \quad (10)$$

$$g = \frac{4}{x^2 Q_{\text{sca}}} \sum_{k=1}^{\infty} \left[\frac{k(k+2)}{k+1} \Re\{a_k a_{k+1}^* + b_k b_{k+1}^*\} + \frac{2k+1}{k(k+1)} \Re\{a_k b_k^*\} \right]. \quad (11)$$

Computational implementation of formulae (7–11) can be found in Bohren & Huffman (1983) and Wiscombe (1979).

2.1.2. Rayleigh scattering

The Rayleigh scattering approximation applies when the grains are very small, i.e. $x \ll 1$, and in addition $x|n| \ll 1$. The above conditions mean that the particles interact with the radiation mainly as electric dipoles with a negligibly small contribution of higher multipoles. The elements of the phase matrix in this case can be obtained from those for Mie scattering [eqs (7)] by retaining in the expansions (8) the terms responsible for the electric dipole interaction, which gives the very simplified expressions (Bohren & Huffman 1983):

$$\begin{aligned} P_1 &= \frac{3}{4}(1 + \cos^2 \Theta_{\text{scat}}), & P_2 &= -\frac{3}{4} \sin^2 \Theta_{\text{scat}}, \\ P_3 &= \frac{3}{2} \cos \Theta_{\text{scat}}, & P_4 &= 0. \end{aligned} \quad (12)$$

The phase matrix \mathcal{P} is a function of the scattering angle Θ_{scat} only, unlike the phase matrix for Mie scattering particles which depends also on grain properties: a , n , and λ . The expressions for the optical efficiencies also become simpler:

$$Q_{\text{sca}} = \frac{8}{3} x^4 \left| \frac{n^2 - 1}{n^2 + 2} \right|^2, \quad Q_{\text{ext}} = 4x \text{Im} \left\{ \frac{n^2 - 1}{n^2 + 2} \right\}, \quad (13)$$

where Im stands for the imaginary part. Note that for Rayleigh scattering by free electrons (Thomson scattering) the elements of the phase matrix are the same as in (12).

2.1.3. Single scattering by a mixture of size-distributed grains

In the previous sections we considered light scattering by a single grain. A dust mixture contains grains made up of various species and a range of sizes. Let $f^i(a)$ be the size distribution function for the i th dust species, that is the number density of grains of type i having sizes within the interval a to $a+da$. The scattering parameters of a volume element is obtained by averaging the single grain scattering over the dust species and the grain-size distributions, which yields the following expressions:

$$P_j(\Theta_{\text{scat}}, \lambda) = \frac{\sum_i \int_0^\infty \pi a^2 Q_{\text{sca}}^i(a, \lambda) P_j^i(\Theta_{\text{scat}}, a, \lambda) f^i(a) da}{\sum_i \int_0^\infty \pi a^2 Q_{\text{sca}}^i(a, \lambda) f^i(a) da}, \quad (14)$$

$$Q_{\text{sca}}(\lambda) = \frac{\sum_i \int_0^\infty \pi a^2 Q_{\text{sca}}^i(a, \lambda) f^i(a) da}{\sum_i \int_0^\infty \pi a^2 f^i(a) da}, \quad (15)$$

$$Q_{\text{ext}}(\lambda) = \frac{\sum_i \int_0^\infty \pi a^2 Q_{\text{ext}}^i(a, \lambda) f^i(a) da}{\sum_i \int_0^\infty \pi a^2 f^i(a) da}, \quad (16)$$

$$g(\lambda) = \frac{\sum_i \int_0^\infty \pi a^2 Q_{\text{sca}}^i(a, \lambda) g(a, \lambda) f^i(a) da}{\sum_i \int_0^\infty \pi a^2 Q_{\text{sca}}^i(a, \lambda) f^i(a) da}, \quad (17)$$

$$\tilde{\omega} = \frac{\sum_i \int_0^\infty \pi a^2 Q_{\text{sca}}^i(a, \lambda) f^i(a) da}{\sum_i \int_0^\infty \pi a^2 Q_{\text{ext}}^i(a, \lambda) f^i(a) da}, \quad (18)$$

where the sum index i runs over all grain species. It is useful to define the scattering and extinction coefficients:

$$k_{\text{sca}}(\lambda) = \sum_i \int_0^\infty \pi a^2 Q_{\text{sca}}^i(a, \lambda) f^i(a) da, \quad (19)$$

$$k_{\text{ext}}(\lambda) = \sum_i \int_0^\infty \pi a^2 Q_{\text{ext}}^i(a, \lambda) f^i(a) da, \quad (20)$$

measured in units of length⁻¹. The inverse quantities k_{sca}^{-1} and k_{ext}^{-1} represent the mean free path of photons for scattering and extinction.

2.2. Scattering by an optically thick dusty slab

In this section we formulate the solution for polarized radiative transfer in a plane-parallel dusty slab. Since dust scattering does not change λ , we omit the explicit dependence of the intensity and polarization on λ .

2.2.1. Mathematical formulation of the problem

Let a dusty slab of optical thickness τ_0 be illuminated by unpolarized radiation incident from a direction θ_0 with a flux F_0 (see Fig. 1). The equation of polarized radiative transfer for the slab is (Chandrasekhar 1960):

$$\mu \frac{d\mathbf{I}(\tau, \mu, \Phi)}{d\tau} = -\mathbf{I}(\tau, \mu, \Phi) + \mathbf{F}(\tau, \mu, \Phi, \mathbf{I}) + \mathbf{S}(\tau, \mu, \Phi), \quad (21)$$

$$\mathbf{F}(\tau, \mu, \Phi, \mathbf{I}) = \frac{\tilde{\omega}}{4\pi} \int_0^{2\pi} \int_{-1}^1 \mathcal{F}(\mu, \Phi, \mu', \Phi') \mathbf{I}(\tau, \mu', \Phi') d\mu' d\Phi', \quad (22)$$

$$\mathbf{S}(\tau, \mu, \Phi) = \frac{\tilde{\omega}}{4\pi} F_0 e^{-\frac{\tau}{\mu_0}} \mathcal{F}(\mu, \Phi, \mu_0, \Phi_0) \mathbf{1} + (1 - \tilde{\omega}) B(T) \mathbf{1}, \quad (23)$$

where \mathbf{I} is the intensity vector of the diffuse radiation at an optical depth τ , going along the direction (θ, Φ) or (μ, Φ) ; where μ is the cosine of zenith angle θ , measured from the upper normal for the upward intensity and from the downward normal for the downward intensity (see Fig. 1); Φ is the azimuthal angle, measured counterclockwise from the projection of the incoming central source beam onto the slab. Note that all scattering quantities depend on the azimuth difference rather than on the azimuth itself. For the incoming beam $\Phi_0 = 0$ and $\mu_0 = \cos \theta_0$.

\mathbf{F} is the scattering integral, expressing the angular transformation of the diffuse radiation due to scattering. \mathcal{F} is the 4-by-4 scattering matrix that relates the intensities of incoming and outgoing radiation, taken in their specific reference planes (see section 2.2.2 for more details).

\mathbf{S} is the source function 4-vector, which includes a ‘pseudo-source’ of single scattered radiation of the central source and unpolarized thermal emission of dust. The latter may be approximated by a black-body radiation B of temperature T . $\mathbf{1}$ is the unity 4-vector (1, 0, 0, 0). Note that in this study we are interested in light scattering in the UV and the optical, where the contribution of the dust thermal emission is negligibly small. We therefore exclude this effect below.

To complete the formulation of the problem, we should specify the boundary conditions for the intensity on the top and bottom faces of the slab (Fig. 1):

$$\mathbf{I}(0, \mu, \Phi) = \mathbf{I}_t^\downarrow(\mu, \Phi), \quad \mathbf{I}(\tau_0, \mu, \Phi) = \mathbf{I}_b^\uparrow(\mu, \Phi), \quad (24)$$

where \mathbf{I}_t^\downarrow (\mathbf{I}_b^\uparrow) is the intensity of diffuse radiation from external sources incident on the top (bottom) of the slab. For a slab with a large optical thickness $\tau_0 \gg 1$, instead of the second boundary condition in (24) we expect that the intensity $\mathbf{I}(\tau, \mu, \Phi)$ at $\tau \rightarrow \infty$ be limited. Note that in this study the intensities \mathbf{I}_t^\downarrow and \mathbf{I}_b^\uparrow of external diffuse radiation in the optical/UV are expected to be negligibly small compared to the intensity of the central source, so we may set them to zero. However, we retain \mathbf{I}_t^\downarrow and \mathbf{I}_b^\uparrow until the end of this section for purpose of generality.

In the following sections we describe how the problem of radiative transfer in a dusty slab can be solved efficiently by the doubling and adding method (Hovenier 1971; Hansen & Travis 1974).

2.2.2. Scattering matrix

The solution of the radiative transfer problem with the doubling and adding method requires a suitable presentation of the scattering matrix \mathcal{F} in terms of angular dependence. Fig. 2 displays the geometry of scattering for any particular point inside the slab. We have an incoming (μ_{in}) and outgoing ($\mu_{\text{out}}, \Phi_{\text{out}}$) beams with the scattering angle between them Θ_{scat} . The theory of single light scattering provides the phase matrix \mathcal{F} as a function of scattering angle [e.g., see (4), (7), (12) and (14)], where here the scattering plane is the natural plane of reference. However, both incoming and outgoing beams have their own reference planes, defined by the Z-axis and a respective beam. Thus, we should perform a few transformations in order to get the scattering matrix \mathcal{F} from the phase matrix \mathcal{P} for any particular beam (Chandrasekhar 1960):

$$\mathcal{F}(\mu_{\text{out}}, \Phi_{\text{out}}, \mu_{\text{in}}) = \mathcal{R}(i_2 - \pi) \mathcal{P}(\cos \Theta_{\text{scat}}) \mathcal{R}(i_1), \quad (25)$$

where \mathcal{R} is the polarization rotation matrix, which is a function of the rotation angle i :

$$\mathcal{R}(i) = \begin{bmatrix} 1 & 0 & 0 & 0 \\ 0 & \cos 2i & -\sin 2i & 0 \\ 0 & \sin 2i & \cos 2i & 0 \\ 0 & 0 & 0 & 1 \end{bmatrix}, \quad (26)$$

Note that this form of \mathcal{R} is valid for the intensity vector representation (I, Q, U, V) , adopted by us. In (25), the matrix \mathcal{R} first transforms the intensity vector of the incident beam from its reference plane $A^{\text{in}}OZ$ into the scattering plane $A^{\text{in}}OA^{\text{out}}$ by rotating through the angle i_1 between the two planes (see Fig. 2). The matrix \mathcal{P} then gives the intensity of the emergent beam, scattered by Θ_{scat} . Finally, the matrix \mathcal{R} transforms the intensity of the emergent beam from the scattering plane into the reference plane of the beam ZOA^{out} by rotating through the angle $i_2 - \pi$. Note that the transformations (25) affect the linear polarization parameters Q and U only, leaving the mean intensity I and circular polarization parameter V unchanged. Only the position angle θ_p of the polarization plane is changed, while the degree of linear polarization $p_l = \sqrt{Q^2 + U^2}/I$ is unchanged. The scattering angle Θ_{scat} , and the angles i_1 and i_2 are calculated from the angles $\mu_{\text{in}}, \mu_{\text{out}}$ and Φ_{out} :

$$\cos \Theta_{\text{scat}} = \mu_{\text{in}}\mu_{\text{out}} + \sqrt{(1 - \mu_{\text{in}}^2)(1 - \mu_{\text{out}}^2)} \cos \Phi_{\text{out}} \quad (27)$$

$$\cos i_1 = \frac{\mu_{\text{out}} \sqrt{1 - \mu_{\text{in}}^2} - \mu_{\text{in}} \sqrt{1 - \mu_{\text{out}}^2} \cos \Phi_{\text{out}}}{\sin \Theta_{\text{scat}}} \quad (28)$$

$$\cos i_2 = \frac{\mu_{\text{in}} \sqrt{1 - \mu_{\text{out}}^2} - \mu_{\text{out}} \sqrt{1 - \mu_{\text{in}}^2} \cos \Phi_{\text{out}}}{\sin \Theta_{\text{scat}}} \quad (29)$$

For computational purposes, it is useful to expand the scattering matrix in a Fourier series in azimuth angle Φ_{out} :

$$\mathcal{F}(\mu_{\text{out}}, \Phi_{\text{out}}, \mu_{\text{in}}) = \sum_{m=0}^{\infty} [\mathcal{F}_m^c(\mu_{\text{out}}, \mu_{\text{in}}) \cos m\Phi_{\text{out}} + \mathcal{F}_m^s(\mu_{\text{out}}, \mu_{\text{in}}) \sin m\Phi_{\text{out}}] \quad (30)$$

Then the Fourier modes \mathcal{F}_m^c and \mathcal{F}_m^s can be calculated with a computationally efficient fast Fourier transform (FFT) for each pair of μ_{in} and μ_{out} :

$$\mathcal{F}_m^c(\mu_{\text{out}}, \mu_{\text{in}}) + i\mathcal{F}_m^s(\mu_{\text{out}}, \mu_{\text{in}}) = \frac{(2 - \delta_{m0})}{N} \sum_{n=0}^{N-1} e^{\frac{2\pi}{N} i n m} \mathcal{F}(\mu_{\text{out}}, \Phi_{\text{out}}^n, \mu_{\text{in}}), \quad (31)$$

where $\Phi_{\text{out}}^n = 2\pi n/N$ for n ranging from 0 to $N-1$, where N must be a power of 2.

In this paper we deal with mixtures of spherical grains for which the phase matrix \mathcal{P} has a simple form (4). For this type of \mathcal{P} , the scattering matrix \mathcal{F} has the following symmetries: 1. Changing the sign of μ_{out} and μ_{in} results in a change of sign of the off-diagonal 2-by-2 blocks of the matrix. Thus, only half the number of μ s is needed to compute the whole scattering matrix. 2. The upper left and lower right 2-by-2 blocks of \mathcal{F} are even functions of Φ_{out} , while the upper right and lower left blocks are odd functions. Thus, the scattering matrix for $\pi < \Phi_{\text{out}} \leq 2\pi$ can be computed from the values for $0 < \Phi_{\text{out}} \leq \pi$.

From the last symmetry it follows that the cosine matrices \mathcal{F}_m^c (sine matrices \mathcal{F}_m^s) have off-diagonal (diagonal) blocks of zeros. This means that we can compose a *single* 4-by-4 scattering matrix for each azimuth mode and pair of zenith angles. Defining a Fourier intensity vector of the form $\bar{\mathbf{I}} = (I^c, Q^c, U^s, V^s)$, containing the cosine azimuth modes of the I and Q Stokes parameters and the sine modes of U and V , then the Fourier scattering matrix can be represented through the Fourier terms from the FFT as

$$\mathcal{F}_m(\mu_{\text{out}}, \mu_{\text{in}}) = \begin{bmatrix} \mathcal{F}_{11}^c & \mathcal{F}_{12}^c & \mathcal{F}_{13}^s & \mathcal{F}_{14}^s \\ \mathcal{F}_{21}^c & \mathcal{F}_{22}^c & \mathcal{F}_{23}^s & \mathcal{F}_{24}^s \\ -\mathcal{F}_{31}^s & -\mathcal{F}_{32}^s & \mathcal{F}_{33}^c & \mathcal{F}_{34}^c \\ -\mathcal{F}_{41}^s & -\mathcal{F}_{42}^s & \mathcal{F}_{43}^c & \mathcal{F}_{44}^c \end{bmatrix}. \quad (32)$$

This form of scattering matrix is especially suitable for efficient implementation of the doubling and adding method (see next subsection).

2.2.3. The doubling and adding method

Fortunately, there is an approach to solve the radiative transfer problem (21–24), which does not require a direct solution of the complicated integro-differential equation (21). This approach is based on the general principle of the linearity of interaction of electromagnetic radiation with a scattering medium. Thus, the intensity of radiation leaving a slab is linearly related to the intensity of the radiation incident on the slab:

$$\mathbf{I}_b^\downarrow = \mathcal{T}^{\downarrow\downarrow} \mathbf{I}_t^\downarrow + \mathcal{R}^{\downarrow\uparrow} \mathbf{I}_b^\uparrow + \mathbf{S}^\downarrow, \quad \mathbf{I}_t^\uparrow = \mathcal{T}^{\uparrow\uparrow} \mathbf{I}_b^\uparrow + \mathcal{R}^{\uparrow\downarrow} \mathbf{I}_t^\downarrow + \mathbf{S}^\uparrow, \quad (33)$$

where $\mathbf{I}_t^{\downarrow,\uparrow}$ ($\mathbf{I}_b^{\downarrow,\uparrow}$) are the intensity vectors on the top (bottom) of the slab, $\mathcal{T}^{\downarrow\downarrow}$ and $\mathcal{T}^{\uparrow\uparrow}$ ($\mathcal{R}^{\downarrow\uparrow}$ and $\mathcal{R}^{\uparrow\downarrow}$) are 4-by-4 transmission (reflection) matrices, and $\mathbf{S}^{\downarrow,\uparrow}$ are the source vectors. The arrows denote the downward (\downarrow) and upward (\uparrow) directions of the beams. In (33) we use a short notation, where the product $\mathbf{J}=\mathcal{A}\mathbf{I}$ of a matrix \mathcal{A} and a vector \mathbf{I} means:

$$\mathbf{J}_i(\mu, \Phi) = \frac{1}{\pi} \int_0^1 \int_0^{2\pi} \left[\sum_{i'=1}^4 \mathcal{A}_{ii'}(\mu, \mu', \Phi - \Phi') \mathbf{I}_{i'}(\mu', \Phi') \right] \mu' d\mu' d\Phi', \quad (34)$$

where the index i , indicating the Stokes parameter, runs from 1 to 4. A similar rule is valid also for a matrix by matrix multiplication, e.g. for $\mathcal{C}=\mathcal{A}\mathcal{B}$

$$\mathcal{C}_{ii'}(\mu, \mu_{\text{in}}, \Phi) = \frac{1}{\pi} \int_0^1 \int_0^{2\pi} \left[\sum_{i''=1}^4 \mathcal{A}_{ii''}(\mu, \mu', \Phi - \Phi') \mathcal{B}_{i''i'}(\mu', \mu_{\text{in}}, \Phi') \right] \mu' d\mu' d\Phi'. \quad (35)$$

Equations (33) can be transformed into a form more suitable for computations by the following steps: 1) expand the matrices and vectors in (33) in Fourier series in azimuth Φ and choose the optimum Fourier basis that would result in decoupling of azimuth modes; 2) discretize zenith angles with a numerical quadrature; 3) rearrange the respective vectors and matrices to their normal forms as one- and two-dimensional objects. Below we describe how these steps are realized for relations (34) and (35).

Expanding the quantities in (34–35) in Fourier series in Φ and choosing a representation for the Fourier components of vectors as (I^c, Q^c, U^s, V^s) and for matrices the one like (32) (see section 2.2.2), decouples the azimuth modes such that for each mode m : $\bar{\mathbf{J}}^m = \bar{\mathcal{A}}^m \bar{\mathbf{I}}^m$ and $\bar{\mathcal{C}}^m = \bar{\mathcal{A}}^m \bar{\mathcal{B}}^m$ where

$$\bar{\mathbf{J}}_i^m(\mu) = 2 \int_0^1 \left[\sum_{i'=1}^4 \bar{\mathcal{A}}_{ii'}^m(\mu_{\text{out}}, \mu') \bar{\mathbf{I}}_{i'}^m(\mu') \right] \mu' d\mu', \quad (36)$$

$$\bar{\mathcal{C}}_{ii'}^m(\mu, \mu_{\text{in}}) = 2 \int_0^1 \left[\sum_{i''=1}^4 \bar{\mathcal{A}}_{ii''}^m(\mu, \mu') \bar{\mathcal{B}}_{i''i'}^m(\mu', \mu_{\text{in}}) \right] \mu' d\mu'. \quad (37)$$

We now discretize the zenith angles using a numerical quadrature, for example, the Gaussian formula. The expressions (36–37) are then transformed into

$$\bar{\mathbf{J}}_{i,j}^m = 2 \sum_{j'=1}^{n_\mu} \sum_{i'=1}^4 \mu_{j'} w_{j'} \bar{\mathcal{A}}_{ii',jj'}^m \bar{\mathbf{I}}_{i',j'}^m, \quad (38)$$

$$\bar{\mathcal{C}}_{ii',jj'}^m = 2 \sum_{j''=1}^{n_\mu} \sum_{i''=1}^4 \mu_{j''} w_{j''} \bar{\mathcal{A}}_{ii'',jj''}^m \bar{\mathcal{B}}_{i''i',j''j'}^m, \quad (39)$$

where the indices j and j' indicate the quadrature angles μ_j and weights w_j , and run from 1 to n_μ , the number of quadrature angles.

Finally, it is useful to rearrange the intensity vector $\bar{\mathbf{I}}_{i,j}^m$ for the m th azimuth mode from a two-dimensional array into a one-dimensional vector \bar{I}_k^m , where $k = i + 4(j - 1)$ is running from 1 to $4n_\mu$. If we then respectively redefine the matrices as, say, $\bar{A}_{kk'}^m = 2\mu_{j'} w_{j'} \bar{\mathcal{A}}_{ii',jj'}^m$ with $k = i + 4(j - 1)$ and $k' = i' + 4(j' - 1)$ instead of $\bar{\mathcal{A}}_{ii',jj'}^m$, the expressions for multiplications of vectors and matrices acquire their natural form:

$$\bar{\mathbf{J}}_k^m = \sum_{k'=1}^n \bar{A}_{kk'}^m \bar{I}_{k'}^m, \quad \bar{\mathcal{C}}_{k,k'}^m = \sum_{k''=1}^n \bar{A}_{kk''}^m \bar{\mathcal{B}}_{k''k'}^m, \quad (40)$$

for $\bar{J}^m = \bar{A}^m \bar{I}^m$ and $\bar{C}^m = \bar{A}^m \bar{B}^m$, respectively, where the vectors have a dimension $n = 4n_\mu$.

We may now return to equations (33) which relates the intensities of the radiations incident onto and emergent from the slab. With the new vector basis and new notation, we may rewrite equations (33) for each azimuth mode (index m is omitted for better clarity) as ordinary vector-matrix relations:

$$\bar{I}_b^\downarrow = \bar{T}^{\downarrow\downarrow} \bar{I}_t^\downarrow + \bar{R}^{\downarrow\uparrow} \bar{I}_b^\uparrow + \bar{S}^\downarrow, \quad \bar{I}_t^\uparrow = \bar{T}^{\uparrow\uparrow} \bar{I}_b^\uparrow + \bar{R}^{\uparrow\downarrow} \bar{I}_t^\downarrow + \bar{S}^\uparrow. \quad (41)$$

Equations (41) are written for the whole slab. Thus, the matrices \bar{T} and \bar{R} and sources \bar{S} for the whole slab provide the solution of our radiative transfer problem. For an optically thin layer $\tau_{\text{in}} \ll 1$, in which single scattering prevails, we may write explicit expressions for the reflection and transmission matrices and the source vector (e.g. Evans & Stephens 1991):

$$|\bar{R}^{\downarrow\uparrow}|_{kk'}^m = \frac{\tilde{\omega} \tau_{\text{in}}}{\mu_j} \frac{1 + \delta_{0m}}{4} w_{j'} |\mathcal{F}_m(\mu_j, -\mu_{j'})|_{ii'}, \quad (42)$$

$$|\bar{R}^{\uparrow\downarrow}|_{kk'}^m = \frac{\tilde{\omega} \tau_{\text{in}}}{\mu_j} \frac{1 + \delta_{0m}}{4} w_{j'} |\mathcal{F}_m(-\mu_j, \mu_{j'})|_{ii'}, \quad (43)$$

$$|\bar{T}^{\downarrow\downarrow}|_{kk'}^m = \delta_{ii'} \delta_{jj'} - \frac{\tau_{\text{in}}}{\mu_j} \left(\delta_{ii'} \delta_{jj'} - \tilde{\omega} \frac{1 + \delta_{0m}}{4} w_{j'} |\mathcal{F}_m(\mu_j, \mu_{j'})|_{ii'} \right), \quad (44)$$

$$|\bar{T}^{\uparrow\uparrow}|_{kk'}^m = \delta_{ii'} \delta_{jj'} - \frac{\tau_{\text{in}}}{\mu_j} \left(\delta_{ii'} \delta_{jj'} - \tilde{\omega} \frac{1 + \delta_{0m}}{4} w_{j'} |\mathcal{F}_m(-\mu_j, -\mu_{j'})|_{ii'} \right), \quad (45)$$

$$|\bar{S}^\downarrow|_k^m = \frac{\tau_{\text{in}}}{\mu_j} |\mathbf{S}(\mu_j)|_i^m, \quad |\bar{S}^\uparrow|_k^m = \frac{\tau_{\text{in}}}{\mu_j} |\mathbf{S}(-\mu_j)|_i^m, \quad (46)$$

where m is the azimuth mode, i, i' are the Stokes parameter indices, j, j' are the quadrature angle indices, $k = i + 4(j - 1)$ and $k' = i' + 4(j' - 1)$ and $|\mathbf{S}|^m$ is the m th Fourier mode of the source term \mathbf{S} [eq. (23)] of the radiative transfer equation.

The next step is to calculate the quantities \bar{T} , \bar{R} and \bar{S} for the whole slab starting from those of the optically thin layer. Applying the relations (41) for two adjacent layers and eliminating the intensities at the common boundary results in the expressions for \bar{T} , \bar{R} and \bar{S} for the layer combined from the two layers. This is the essence of *the adding method*. It thus allows us to get the properties of the combined layer through the properties of the top (\top) and the bottom (\perp) layers:

$$\begin{aligned} \bar{R}^{\downarrow\uparrow} &= \bar{R}_\perp^{\downarrow\uparrow} + \bar{T}_\perp^{\downarrow\downarrow} \bar{M}^{\downarrow\downarrow} \bar{R}_\top^{\downarrow\uparrow} \bar{T}_\perp^{\uparrow\uparrow}, & \bar{R}^{\uparrow\downarrow} &= \bar{R}_\top^{\uparrow\downarrow} + \bar{T}_\top^{\uparrow\uparrow} \bar{M}^{\uparrow\uparrow} \bar{R}_\perp^{\uparrow\downarrow} \bar{T}_\top^{\downarrow\downarrow}, \\ \bar{T}^{\downarrow\downarrow} &= \bar{T}_\perp^{\downarrow\downarrow} \bar{M}^{\downarrow\downarrow} \bar{T}_\top^{\downarrow\downarrow}, & \bar{T}^{\uparrow\uparrow} &= \bar{T}_\top^{\uparrow\uparrow} \bar{M}^{\uparrow\uparrow} \bar{T}_\perp^{\uparrow\uparrow}, \\ \bar{S}^\downarrow &= \bar{S}_\perp^\downarrow + \bar{T}_\perp^{\downarrow\downarrow} \bar{M}^{\downarrow\downarrow} (\bar{S}_\top^\downarrow + \bar{R}_\top^{\downarrow\uparrow} \bar{S}_\perp^\uparrow), & \bar{S}^\uparrow &= \bar{S}_\top^\uparrow + \bar{T}_\top^{\uparrow\uparrow} \bar{M}^{\uparrow\uparrow} (\bar{S}_\perp^\uparrow + \bar{R}_\perp^{\uparrow\downarrow} \bar{S}_\top^\downarrow), \\ \bar{M}^{\downarrow\downarrow} &= \left(1 - \bar{R}_\top^{\downarrow\uparrow} \bar{R}_\perp^{\uparrow\downarrow}\right)^{-1}, & \bar{M}^{\uparrow\uparrow} &= \left(1 - \bar{R}_\perp^{\uparrow\downarrow} \bar{R}_\top^{\downarrow\uparrow}\right)^{-1}, \end{aligned} \quad (47)$$

where $\bar{M}^{\downarrow\downarrow, \uparrow\uparrow}$ are the matrices which represent multiple reflection factors. Physically, the formulae (47) may be interpreted through the concept of multiple reflected beams (Hansen & Travis 1974). The special case of the adding method, when formulae (47) are applied to two *identical* layers with the same optical thickness τ and dust composition (albedo $\tilde{\omega}$, and scattering matrix \mathcal{F}), is called *the doubling method*.

Thus, in order to calculate the matrices \bar{R} , \bar{T} and source vectors \bar{S} for a general, inhomogeneous, and optically thick slab, one needs to: 1. Divide the slab to thinner layers, which could be approximated as homogeneous; the number and thicknesses of the layers are chosen, depending on the required accuracy. 2. For each homogeneous layer, apply the doubling method, that is, first calculate the quantities \bar{R} , \bar{T} and

\bar{S} for a sufficiently optically thin sublayer, normally $\tau_{\text{in}} = 10^{-6} - 10^{-5}$, with the formulae (42–46). Then build up the quantities \bar{R} , \bar{T} and \bar{S} for the whole layer in a doubling manner using equations (47). 3. Build up the quantities \bar{R} , \bar{T} and \bar{S} for the whole slab by reapplying the adding formulae (47) for all the layers of the slab.

Note that the pseudo-source of the single-scattered radiation from the central source [equation (23)] is exponentially dependent on the optical depth, thus violating the homogeneity of the layer, required for doubling to work. In this case, however, it is possible to use Wiscombe’s (1976) extension of the doubling method, incorporating this kind of sources.

Once the matrices \bar{R} , \bar{T} and sources \bar{S} are computed, we may calculate the Fourier modes of the intensities of the radiation emergent from the slab, $\bar{I}_{\text{b}[i,j]}^{\downarrow m}$ and $\bar{I}_{\text{t}[i,j]}^{\uparrow m}$, with formulae (41). To get the intensities themselves, we should convert the Fourier modes back into the azimuth space:

$$\begin{aligned} \mathbf{I}_{\text{b}[i,j]}^{\downarrow}(\Phi) &= \sum_{m=0}^{n_m} \bar{I}_{\text{b}[i,j]}^{\downarrow m} \cdot \begin{cases} \cos m\Phi, & i = 1, 2 \\ \sin m\Phi, & i = 3, 4 \end{cases}, \quad i = 1, \dots, 4, \quad j = 1, \dots, n_\mu, \\ \mathbf{I}_{\text{t}[i,j]}^{\uparrow}(\Phi) &= \sum_{m=0}^{n_m} \bar{I}_{\text{t}[i,j]}^{\uparrow m} \cdot \begin{cases} \cos m\Phi, & i = 1, 2 \\ \sin m\Phi, & i = 3, 4 \end{cases}, \quad i = 1, \dots, 4, \quad j = 1, \dots, n_\mu, \end{aligned} \quad (48)$$

where i is the Stokes parameter index, j is the quadrature zenith angle index and n_m is the number of azimuth modes.

Using relations (41), we may derive expressions for the intensity vectors \bar{I}^{\downarrow} and \bar{I}^{\uparrow} at any depth inside the slab

$$\bar{I}^{\downarrow} = \bar{M}^{\downarrow\downarrow} \left[\bar{S}_{\top}^{\downarrow} + \bar{T}_{\top}^{\downarrow\downarrow} \bar{I}_{\text{t}}^{\downarrow} + \bar{R}_{\top}^{\downarrow\uparrow} \left(\bar{S}_{\perp}^{\uparrow} + \bar{T}_{\perp}^{\uparrow\uparrow} \bar{I}_{\text{b}}^{\uparrow} \right) \right], \quad \bar{I}^{\uparrow} = \bar{M}^{\uparrow\uparrow} \left[\bar{S}_{\perp}^{\uparrow} + \bar{T}_{\perp}^{\uparrow\uparrow} \bar{I}_{\text{b}}^{\uparrow} + \bar{R}_{\perp}^{\uparrow\downarrow} \left(\bar{S}_{\top}^{\downarrow} + \bar{T}_{\top}^{\downarrow\downarrow} \bar{I}_{\text{t}}^{\downarrow} \right) \right], \quad (49)$$

where the matrices \bar{T} and \bar{R} and sources \bar{S} correspond to the layers above (\top) and below (\perp) the level, and the matrices \bar{M} are defined through matrices \bar{R} in (47). The Fourier modes of the intensities \bar{I}^{\downarrow} and \bar{I}^{\uparrow} can be converted into the azimuth space by means of the formulae like (48).

The polarization properties of the radiation reflected by the slab are represented by the degree of linear polarization, $p_{\text{lin}}^{\text{t}}$, the position angle, $\theta_{\text{p}}^{\text{t}}$, and the degree of circular polarization, $p_{\text{cir}}^{\text{t}}$,

$$p_{\text{lin}}^{\text{t}} = \frac{\sqrt{Q_{\text{t}}^2 + U_{\text{t}}^2}}{I_{\text{t}}}, \quad \theta_{\text{p}}^{\text{t}} = \frac{1}{2} \arctan \frac{U_{\text{t}}}{Q_{\text{t}}}, \quad p_{\text{cir}}^{\text{t}} = \frac{V_{\text{t}}}{I_{\text{t}}}, \quad (50)$$

where $\mathbf{I}_{\text{t}}^{\uparrow} = (I_{\text{t}}, Q_{\text{t}}, U_{\text{t}}, V_{\text{t}})$, $\cos 2\theta_{\text{p}}^{\text{t}}$ should have the same sign as Q_{t} , and all the quantities in (50) are written for the radiation, reflected from the top. Similar expressions may be written for the transmitted radiation, escaping from the bottom.

Other useful characteristics of the radiation leaving the slab are the fluxes of the radiation emergent from top and bottom:

$$\begin{aligned} \mathbf{F}_{\text{t}[i]}^{\uparrow} &= \int_0^{2\pi} \int_0^1 \mathbf{I}_{\text{t}[i]}^{\uparrow}(\mu, \Phi) \, d\mu \, d\Phi = 2\pi \sum_{j=1}^{n_\mu} w_j \mu_j \bar{I}_{\text{t}[i,j]}^{\uparrow 0}, \quad i = 1, \dots, 4, \\ \mathbf{F}_{\text{b}[i]}^{\downarrow} &= \int_0^{2\pi} \int_0^1 \mathbf{I}_{\text{b}[i]}^{\downarrow}(\mu, \Phi) \, d\mu \, d\Phi = 2\pi \sum_{j=1}^{n_\mu} w_j \mu_j \bar{I}_{\text{b}[i,j]}^{\downarrow 0}, \quad i = 1, \dots, 4, \end{aligned} \quad (51)$$

where only zero-th azimuth mode of respective intensity need be used. Only the Stokes parameters I and Q ($i=1,2$) of the fluxes $\mathbf{F}_{\text{t}[i]}^{\uparrow}$ and $\mathbf{F}_{\text{b}[i]}^{\downarrow}$ can be non-zero. The fraction of the incident flux which is reflected is called the plane albedo:

$$A(\mu_0) = \frac{\mathbf{F}_{\text{t}[0]}^{\uparrow}}{F_0}, \quad (52)$$

where F_0 is the flux of the incident unpolarized radiation of the central source, coming at zenith angle μ_0 .

2.3. Scattering by an optically thick dusty sphere

In this section we apply the dusty slab calculations to calculate the scattering from a dusty sphere. The sphere is assumed to have $\tau \gg 1$, so that the thickness of the $\tau \sim 1$ surface layer is much smaller than the radius of the sphere, and thus every surface element can be treated with the "local slab" approximation. As in the slab calculations, we assume that the illumination source distance is much larger than the radius of the sphere, so the incident rays are assumed to be parallel. The geometry of the scattering is schematically represented at Fig. 3. The radius of the sphere is R_s . The flux of the incoming unpolarized radiation from the central source is F_0 . The coordinate system is chosen in such a way that the X axis is directed toward the observer, and the direction of the beam incident from the source is parallel to the XY plane. The position of any point S on the sphere surface is then defined by two angles: zenith angle θ measured from the Z axis and azimuth Φ measured from the X axis. The angle between the directions from the source and to the observer, Θ_{obs} , is the same at any point on the sphere surface, and it is equal to the scattering angle for single scattering.

The angular parameters of the incident and emergent beams, are shown at Fig. 2:

$$\cos \theta_{\text{in}}(\theta, \Phi, \Theta_{\text{obs}}) = \mu_{\text{in}} = -\sin \theta \cos(\Phi + \Theta_{\text{obs}}), \quad (53)$$

$$\cos \theta_{\text{out}}(\theta, \Phi) = \mu_{\text{out}} = \sin \theta \cos \Phi, \quad (54)$$

$$\cos \Phi_{\text{out}}(\theta, \Phi, \Theta_{\text{obs}}) = \frac{\cos \Theta_{\text{obs}} + \mu_{\text{in}} \mu_{\text{out}}}{\sqrt{(1 - \mu_{\text{in}}^2)(1 - \mu_{\text{out}}^2)}}. \quad (55)$$

The intensity vector \mathbf{I}_{sph} of the radiation scattered by the sphere is calculated by integrating the local intensity \mathbf{I}^{loc} over the illuminated part of the sphere, as seen from the observer direction:

$$\mathbf{I}_{\text{sph}} = \int \int_S \mathbf{I}^{\text{loc}} \mu_{\text{out}} dS, \quad (56)$$

where \mathbf{I}^{loc} is the local intensity of the emergent radiation, as measured in the observer reference plane, chosen here to be the scattering plane $A^{\text{in}}SA^{\text{out}}$. \mathbf{I}^{loc} is derived from the local emergent intensity, \mathbf{I}_t^\uparrow [see equation (48)], defined with respect to the local (meridian) reference plane, by rotating it with the matrix \mathcal{R} through a respective angle ψ :

$$\mathbf{I}^{\text{loc}} = \mathcal{R}(\psi) \mathbf{I}_t^\uparrow. \quad (57)$$

Substituting into (56) and (57) the expressions for the surface element $dS = R_s^2 \sin \theta d\theta d\Phi$ and μ_{out} from (54), we obtain

$$\mathbf{I}_{\text{sph}}(R_s, \Theta_{\text{obs}}) = R_s^2 \int_{\frac{\pi}{2} - \Theta_{\text{obs}}}^{\frac{\pi}{2}} \cos \Phi d\Phi \int_0^\pi \sin^2 \theta d\theta \cdot \mathbf{I}^{\text{loc}}(\theta, \Phi, \Theta_{\text{obs}}), \quad (58)$$

$$\mathbf{I}^{\text{loc}}(\theta, \Phi, \Theta_{\text{obs}}) = \mathcal{R}[\psi(\theta, \Phi)] \cdot \mathbf{I}_t^\uparrow(\theta, \Phi, \Theta_{\text{obs}}), \quad (59)$$

where the integration limits correspond to the illuminated part of the sphere, as seen by the observer. The intensity \mathbf{I}_t^\uparrow depends on θ , Φ and Θ_{obs} through μ_{in} , μ_{out} and Φ_{out} (eqs 53–55). ψ is the rotation angle defined through its cosine and sine:

$$\cos \psi = \frac{\sin \theta \sin \Phi}{\sqrt{1 - \mu_{\text{out}}^2}}, \quad \sin \psi = \frac{-\cos \theta}{\sqrt{1 - \mu_{\text{out}}^2}} \quad (60)$$

It is simple to show that from the specific azimuthal dependences of various Stokes parameters (see eqs 48) one gets symmetry relations for the intensities at the surface points, located symmetrically with respect to the equatorial plane XOY :

$$\begin{aligned} \mathbf{I}_{t[i]}^\uparrow(\theta, \Phi, \Theta_{\text{obs}}) &= \mathbf{I}_{t[i]}^\uparrow(\pi - \theta, \Phi, \Theta_{\text{obs}}), & i = 1, 2, \\ \mathbf{I}_{t[i]}^\uparrow(\theta, \Phi, \Theta_{\text{obs}}) &= -\mathbf{I}_{t[i]}^\uparrow(\pi - \theta, \Phi, \Theta_{\text{obs}}), & i = 3, 4. \end{aligned} \quad (61)$$

Note that these relations are also valid for the intensities \mathbf{I}^{loc} . Thus, using relations (61) for the rotated intensities \mathbf{I}^{loc} , we may rewrite the expression (58) for each Stokes parameter of \mathbf{I}_{sph} as follows:

$$I_{\text{sph}}(R_s, \Theta_{\text{obs}}) = 2R_s^2 \int_{\frac{\pi}{2} - \Theta_{\text{obs}}}^{\frac{\pi}{2}} \cos \Phi \, d\Phi \int_0^{\frac{\pi}{2}} \sin^2 \theta \, d\theta \cdot \mathbf{I}_{[0]}^{\text{loc}}(\theta, \Phi, \Theta_{\text{obs}}), \quad (62)$$

$$Q_{\text{sph}}(R_s, \Theta_{\text{obs}}) = 2R_s^2 \int_{\frac{\pi}{2} - \Theta_{\text{obs}}}^{\frac{\pi}{2}} \cos \Phi \, d\Phi \int_0^{\frac{\pi}{2}} \sin^2 \theta \, d\theta \cdot \mathbf{I}_{[1]}^{\text{loc}}(\theta, \Phi, \Theta_{\text{obs}}), \quad (63)$$

$$U_{\text{sph}}(R_s, \Theta_{\text{obs}}) = V_{\text{sph}}(R_s, \Theta_{\text{obs}}) = 0. \quad (64)$$

These symmetry relations imply that the total circular polarization of light scattered by a sphere is zero (just as there is no circular polarization from a single scattering by a spherical grain), and the linear polarization is

$$p_{\text{sph}}(\Theta_{\text{obs}}) = \frac{Q_{\text{sph}}}{I_{\text{sph}}}. \quad (65)$$

The ratio of the total flux scattered by the sphere to the incident flux ($F_0 \cdot \pi R_s^2$) is the so-called spherical albedo:

$$A_{\text{sph}} = 2 \int_0^1 A(\mu_0) \mu_0 \, d\mu_0, \quad (66)$$

where $A(\mu_0)$ is the plane albedo defined by means of eq. (52).

Once the local intensity vector \mathbf{I}^{loc} (I_{loc} , Q_{loc} , U_{loc} , V_{loc}) is calculated as a function of the surface coordinates (θ, Φ) , one can build maps of both linear and circular polarization. For this purpose we define the following parameters: the local degree of linear polarization p_1^{loc} , the local position angle θ_p^{loc} , and the local degree of circular polarization p_c^{loc} in a usual manner:

$$p_1^{\text{loc}}(\theta, \Phi, \Theta_{\text{obs}}) = \frac{\sqrt{Q_{\text{loc}}^2(\theta, \Phi, \Theta_{\text{obs}}) + U_{\text{loc}}^2(\theta, \Phi, \Theta_{\text{obs}})}}{I_{\text{loc}}(\theta, \Phi, \Theta_{\text{obs}})}, \quad (67)$$

$$\theta_p^{\text{loc}}(\theta, \Phi, \Theta_{\text{obs}}) = \frac{1}{2} \arctan \frac{U_{\text{loc}}(\theta, \Phi, \Theta_{\text{obs}})}{Q_{\text{loc}}(\theta, \Phi, \Theta_{\text{obs}})}, \quad (68)$$

$$p_c^{\text{loc}}(\theta, \Phi, \Theta_{\text{obs}}) = \frac{V_{\text{loc}}(\theta, \Phi, \Theta_{\text{obs}})}{I_{\text{loc}}(\theta, \Phi, \Theta_{\text{obs}})}. \quad (69)$$

3. Results

This section describes extensive numerical results obtained with the codes PRT and PRT-SPH, which are described in detail in the Appendix. The objects we model here are optically thick dusty slabs and spheres, composed of a simple mixture of bare spherical graphite and silicate grains having a power-law size distribution $f(a) \sim a^{-3.5}$ for radii 0.005–0.25 μm . This model was introduced by Mathis, Rumpl,

& Nordsieck (1977; hereafter MRN) for interstellar medium dust and further developed by Draine & Lee (1984). It served as a standard model for interstellar dust for many years, though recent new observational data suggest that other dust models may be more viable (see Zubko 1999 for a short review). However, a dust model which is consistent with all the new data is still not established, and we therefore chose to make our first exploration of the effects of optical depth and geometrical configuration using the standard MRN model.

3.1. Single scattering by MRN dust

Figure 4 displays the single scattering albedo and the phase function asymmetry parameter, g , of MRN dust for the wavelength range $0.05\text{--}1\ \mu\text{m}$, used throughout this section. The optical constants of graphite and ‘astronomical’ silicate were taken from Laor & Draine (1993). The albedo is typically $0.4\text{--}0.6$, with a significant drop at $\lambda < 2500\ \text{\AA}$, whereas g generally increases towards smaller λ . The scattering phase function becomes significantly more forward peaked at smaller λ due to the increasing size parameter. Figure 5 demonstrates that the extinction curve of MRN dust reproduces quite well the mean Galactic extinction curve.

Figure 6 summarizes the scattering characteristics of optically thin MRN dust as a function of λ and as a function of Θ_{scat} . The scattered spectrum is bluer than the incident spectrum at all Θ_{scat} for $\lambda > 2500\ \text{\AA}$ since the scattering cross section increases with decreasing λ . The “bluening” of the scattered flux is most prominent at small Θ_{scat} since the scattering gets more forward peaked with decreasing λ (Fig. 4). The bluening effect stops below $2500\ \text{\AA}$ for $\Theta_{\text{scat}} \geq 30^\circ$ due to the sudden drop in the albedo (Fig. 4), compounded by the rising g . A rather strong scattering peak due to graphite grains is predicted at $\lambda \sim 2200\ \text{\AA}$ for large Θ_{scat} . Another similar, but much broader peak is expected in the far UV ($700\text{--}1000\ \text{\AA}$) due to both graphite and silicate grains.

The polarization spectrum $p(\lambda)$ displays a more complicated wavelength dependence than the intensity, and it is also strongly dependent on Θ_{scat} . Overall, $p(\lambda)$ tend to decrease from $1\ \mu\text{m}$ to $\sim 2000\ \text{\AA}$, and then tends to sharply increase to the far UV. The polarization plane is generally at right angle to the scattering plane (defined by the incoming and outgoing rays), excluding a small range of angles at large Θ_{scat} ($150^\circ - 170^\circ$), where the polarization rotates by 90° , but only over a small range of λ , and with a very small amplitude. The feature around $\lambda=0.14\ \mu\text{m}$ is also predicted for the extinction curve, but it is not observed (Fig. 5). Thus, this feature is most likely an artifact due to imperfect optical constants of silicate, as discussed by Kim & Martin (1995).

The angular dependence of the scattered intensity demonstrates how the scattering becomes strongly forward peaked with decreasing λ . At the longest wavelengths the phase function tends towards the Rayleigh scattering phase function limit. The angular dependence of p always shows a clear peak at $\Theta_{\text{scat}}=80\text{--}100^\circ$. The shape of this peak is not always symmetric, and as mentioned above, p rotates by 90° (indicated by negative values in the plot) for a small range of λ at large Θ_{scat} .

3.2. Optically thick dusty slab

The scattering characteristics for an optically thick dusty slab depend on three angles: $\theta_{\text{in}}(\mu_{\text{in}})$, $\theta_{\text{out}}(\mu_{\text{out}})$ and Φ_{out} (see Figure 2), rather than just Θ_{scat} as in the optically thin case.

Figure 7 shows the intensity I_t as a function of λ for various values of μ_{in} , μ_{out} , and Φ_{out} . At a given Φ_{out} , μ_{in} , and λ , I_t decreases with increasing μ_{out} , i.e. the surface brightness of the slab decreases towards face on view. This effect is largest when μ_{in} is smallest, since then the radiation is incident close to edge on, penetrates only a thin layer at the top of the slab, and this layer is effectively optically thin, and of low surface brightness when viewed close to face on. The dependence on λ is generally weak longward of 2200 Å, with a significant drop at $\lambda < 2200$ Å due to the albedo drop.

Figure 8 shows $p_{\text{lin}}^t(\lambda)$ for the same parameters. As shown later, the main physical parameter which determines the shape of $p_{\text{lin}}^t(\lambda)$ is Θ_{scat} , which is now a function of μ_{in} , μ_{out} , and Φ_{out} . For example, when μ_{in} is very close to edge on (0.0672), and $\Phi_{\text{out}} = 90^\circ$, then all values of μ_{out} correspond to $\Theta_{\text{scat}} \sim 90^\circ$, and all the $p_{\text{lin}}^t(\lambda)$ curves in this subpanel nearly overlap.

Figure 9 shows the position angle θ_p^t for the same parameters. The position angle is almost always fixed at right angle to the plane defined by the incoming and outgoing rays. The plane used to define θ_p^t in the optically thick case is defined by the slab normal and the outgoing ray, and thus θ_p^t simply represents the angle between this plane and the incident/outgoing rays plane. However, this figure is shown since θ_p^t jumps by 90° for certain combinations of parameters. This effect is similar to the rotation seen in the optically thin case, and occurs here also for large values of Θ_{scat} .

Figure 10 shows the circular polarization p_{cir}^t for the same parameters. The amplitude of p_{cir}^t is generally well below 1%, and it can be both negative and positive. When $\Phi_{\text{out}}=0^\circ$ or 180° , $p_{\text{cir}}^t=0$ for any μ_{in} and μ_{out} .

The doubling method does not allow one to separate directly the contribution of single and multiple scattering to the total polarization. To explore this point we plot in Figure 11 $p_{\text{lin}}^t(\lambda)$ for complete backscattering ($\Theta_{\text{scat}} = 180^\circ$), which occurs for $\mu_{\text{in}}=\mu_{\text{out}}$ and $\Phi_{\text{out}} = 180^\circ$. In this case single scattering produces no polarization, and the observed polarization is due to multiple scattering only. The typical values of $p_{\text{lin}}^t(\lambda)$ are 1–4%, and the polarization plane is generally parallel to the slab normal (see right panel of Figure 2). Figure 8 indicates that $p_{\text{lin}}^t(\lambda)$ is typically 10–20 times larger than obtained for multiple scattering, and thus it must be dominated by the single scattering contribution. The low multiple scattering polarization is explained by the fact that the radiation field incident on a grain from multiple scattering is much more isotropic than the primary source illumination. Most of the photons incident on the grain following multiple scattering move roughly parallel to the slab surface, and thus they produce a polarization which is generally parallel to the slab normal.

Figure 12 displays the slab albedo $A(\lambda)$. Its wavelength dependence is very similar to the MRN dust albedo (Fig. 4), but the amplitude is significantly lower. At very small μ_{in} the scattering layer is optically thin for most μ_{out} , and most photons that scatter upwards escape, while most photons scattered downward are absorbed, yielding a slab albedo which is very close to one half the dust albedo. As μ_{in} increases the scattering layer becomes optically thicker for all μ_{out} , and the escaping fraction decreases. This effect becomes most prominent at the shortest wavelengths where the scattering becomes most forward peaked, which decreases the probability the photons will be scattered back and escape. Thus, the typical dusty slab albedo falls from $\sim 10\%$ in the optical to only a few % in the far UV.

3.3. Optically thick dusty sphere

Figures 13–15 present maps of the linear and circular polarization at $\lambda=0.05, 0.2124$ and $1 \mu\text{m}$ for a range of Θ_{obs} . The illuminated part of the sphere extends to the terminator at $\Phi_{\text{term}} = \frac{\pi}{2} - \Theta_{\text{obs}}$, which corresponds to a fractional projected illuminated area of $\delta(\Theta_{\text{obs}}) = \frac{1}{2}(1 - \cos \Theta_{\text{obs}})$.

The polarization at each point on the surface is generally largest at $\Theta_{\text{obs}} \simeq 90^\circ$, and at most angles it is aligned at right angle to the scattering plane (i.e. along the axis of the sphere), indicating that it is dominated by single scattering. When $\Theta_{\text{obs}}=180^\circ$ the polarization tends to be aligned radially, indicating it originates in multiple scattering which produces a polarization aligned along the local surface normal (see previous section). The integrated polarization at $\Theta_{\text{obs}}=180^\circ$ is obviously zero, as expected from symmetry. A similar effect occurs at very small Θ_{obs} , where the single scattering polarization amplitude becomes very small, and the polarization can be dominated by multiple scattering. For example, when $\Theta_{\text{obs}}=2^\circ$ and $\lambda=1 \mu\text{m}$ the polarization pattern is radial, and thus dominated by multiple scattering. But, at $\lambda=500 \text{ \AA}$ the polarization pattern remains parallel due to the lower dust albedo, and increased forward scattering, both of which suppress the effect of multiple scattering.

The circular polarization maps typically consist of four regions with two boundaries across which the polarization changes sign, one is the equatorial line, $\theta_{\text{b}}=0$, and the other is the meridional line $\Phi_{\text{b}} = \frac{1}{2}(\pi - \Theta_{\text{obs}})$ (see Figures 13–15). There is a critical angle $\Theta_{\text{obs}}^{\text{crit}} \simeq 60^\circ - 80^\circ$ at which the circular polarization changes sign at all positions, and there is also a critical wavelength $\lambda^{\text{crit}} \simeq 700 \text{ \AA}$, at which a similar sign change occurs. The local amplitude of p_c reaches a maximum of around 1–2 % at $\Theta_{\text{obs}}=110^\circ\text{--}130^\circ$. At $\Theta_{\text{obs}}=0^\circ$ or 180° , $p_c=0$ throughout the whole illuminated disk, as expected from symmetry.

Figure 16 shows the integrated scattering characteristics of an optically thick dusty sphere as a function of λ and Θ_{obs} . This figure is analogous to Fig. 6 which shows the scattering characteristics of optically thin dust. The increase in $I_{\text{sph}}(\lambda, \Theta_{\text{obs}})$ with increasing Θ_{obs} is due to the increasing illuminated fraction of the sphere. The increase in $I_{\text{sph}}(\lambda, \Theta_{\text{obs}})$ is smallest at the shortest λ because of the counteracting effect of the scattering phase function, which enhances the scattering at small Θ_{obs} . Note that the feature related to the 2200 \AA extinction bump changes its nature from an emission peak at $\lambda \sim 2500 \text{ \AA}$ at large Θ_{obs} , to a weak absorption trough at $\lambda \sim 2100 \text{ \AA}$ at small Θ_{obs} . The wavelength dependence of p_{sph} looks quite similar to the one for optically thin dust, as further discussed below.

The spherical albedo as a function of λ is displayed in Figure 12. It is generally rather low, and drops from $\sim 11\%$ in the near IR to $\sim 4\%$ in the far UV. The spherical albedo is very similar to the albedo of a slab illuminated at $\mu_{\text{in}} = 0.5$, which is the mean value of μ_{in} for a sphere.

Figure 17 provides a direct comparison of scattering from optically thin dust and from an optically thick sphere, where in both cases the observed spectrum depends on a single angle only (Θ_{scat} , or Θ_{obs}). The spectrum of the scattered light is quite different in the two cases. It is significantly blued in the optically thin case at $\lambda > 2200 \text{ \AA}$, and is generally grey scattered in the optically thick case. Optically thin scattering produces a broad deep centered at $\lambda \sim 1500 \text{ \AA}$, while the optically thick dust scattering shows an overall drop at $\lambda < 2200 \text{ \AA}$, with only a mild rise towards 1000 \AA . In sharp contrast to the intensity dependence on optical depth, $p(\lambda)$ is remarkably similar for both cases. The shape of $p(\lambda)$ is almost identical for both cases at a given Θ , and only the amplitudes of $p(\lambda)$ differ by $\sim 10\%$. This similarity reflects the overall small contribution of multiple scattering to the polarization. The Θ dependence of $p(\lambda)$ is also very similar for the optically thin and thick cases. Thus, $I(\lambda)$ serves as a sensitive probe of the optical depth

of the scattering dust, while $p(\lambda)$ serves as an optical depth independent probe of the dust properties and scattering geometry.

4. Conclusions

We present extensive numerical results on the scattering and polarization properties of dust in various configurations. The solution of the polarized radiative transfer problem is carried out using the adding-doubling method, which applies to a plane parallel configuration. This method can be extended to other optically thick geometries by an appropriate integration over their surface. The numerical implementation is made with a set of codes which take as input a specified set of dielectric functions, calculates the scattering phase matrix for a spherical grain of a given size and composition, and integrates the matrix elements over a specified dust model to obtain the dust scattering phase matrix. The dust scattering phase matrix is the input for the numerical code which implements the doubling-adding method, and outputs the Stokes vectors for a large grid of incident and outgoing rays. This grid provides the input for the final code which integrates the slab results over the surface of a sphere and outputs the Stokes vector as a function of scattering angle from the sphere.

The accuracy of the radiative transfer calculations was verified by comparison to analytic results available for a Rayleigh scattering atmosphere, and by comparison to earlier calculations for an MRN dusty sphere. We also used our code to obtain a simple analytic approximation for the flux transmitted through an electron scattering slab, which is accurate to 4% at all τ .

In this paper we used this set of codes to explore the effects of optical depth, scattering angles, and dust configuration (slab or sphere), on the scattering and polarization properties of MRN dust from the near IR ($1 \mu m$) to the far UV (500 \AA). We find that the scattered spectrum provides a sensitive probe for the optical depth of the scattering medium, while the polarization spectrum provides a probe of the dust model and scattering geometry, which is practically independent of optical depth. We provide maps of the linear and circular polarization for scattering from a sphere which may be useful for interpreting imaging spectropolarimetry of scattered light in a variety of Galactic and extragalactic objects from the near IR to the far UV.

The MRN model assumes spherical grains, but the fact that extinction in the Galaxy induces polarization clearly indicates that this assumption is not valid. How does the grains non sphericity and alignment affects the scattering polarization? An accurate answer requires detailed calculations which are beyond the scope of this paper. However, we note that the amplitude of polarization induced by transmission through an optical depth of unity ($\leq 3\%$) is about an order of magnitude smaller than the polarization induced by scattering. Thus, it is plausible to assume that the observed level of non sphericity and alignment will not have a major effect on the results presented here.

In a following paper we explore the polarization signature of various dust models over a range of possible compositions and grain size distributions. We also plan to extend our code to handle other plausible geometries, such as a dusty disk and a dusty torus. We plan to make these codes publicly available, which will provide a useful tool for interpreting available spectropolarimetry results, and in particular, help justify new observations that can teach us about the properties of dust in various Galactic and extragalactic environments.

This research was funded by a grant from Israel Science Foundation. We thank the referee John Mathis

for pointing out a couple of errors, and for many helpful comments.

REFERENCES

- Antonucci, R., 1993, *ARA&A*, 31, 473
- Antonucci, R., & Miller, J. S. 1985, *ApJ*, 297, 621
- Balick, B., Alexander, J., Hajian, A. R., Terzian, Y., Perinotto, M., & Patriarchi, P. 1998, *AJ*, 116, 360
- Bally, J., Sutherland, R. S., Devine, D., & Johnstone, D. 1998, *AJ*, 116, 293
- Bohren, C.F., & Huffman, D.R. 1983, *Absorption and Scattering of Light by Small Particles* (New York: Wiley-Interscience)
- Brotherton, M. S., Wills, B. J., Dey, A., van Breugel, W., & Antonucci, R. 1998, *ApJ*, 501, 110
- Burkert, A., & O'Dell, C. R., *ApJ*, 503, 792
- Calzetti, D., Bohlin, R. C., Gordon, K. D., Witt, A. N., & Bianchi, L. 1995, *ApJ*, 446, L97
- Capetti, A., Axon, D. J., Macchetto, F., Sparks, W. B., & Boksenberg, A. 1996, *ApJ*, 466, 169
- Cardelli, J.A., Clayton, G.C., & Mathis, J.S. 1989, *ApJ*, 345, 245
- Chandrasekhar, S. 1960, *Radiative Transfer* (New York: Dover)
- Chiang, E. I., & Goldreich, P. 1997, *ApJ*, 490, 368
- Cimatti, A., di Serego Alighieri, S., Vernet, J., Cohen, M. H., & Fosbury, R. A. E. 1998, *ApJ*, 499, L21
- Code, A.D., et. al. 1996, *BASS*, 188, 57.12
- Code, A.D., & Whitney, B.A. 1995, *ApJ*, 441, 400
- Cohen, M. H., et al. 1995, *ApJ*, 448, L77
- De Breuck, C., Brotherton, M. S., Tran, H. D., van Breugel, W., & Rottgering, H. J. A. 1998, *ApJ*, 116, 13
- Dey, A., Cimatti, A., van Breugel, B., Antonucci, R., & Spinrad, H. 1996, *ApJ*, 465, 157
- Dolginov, A.Z., Gnedin, Yu.N., & Silant'ev, N.A. 1995, *Propagation and Polarization of Radiation in Cosmic Media* (Amsterdam: Gordon & Breach)
- Draine, B.T., & Lee, H.M. 1984, *ApJ*, 285, 89
- Evans, K.F., & Stephens, G.L. 1991, *J. Quant. Spectrosc. Radiat. Transfer*, 46, 413
- Fischer, O., Henning, Th., & Yorke, H.W. 1994, *A&A*, 284, 187
- Forsythe, G.E., Malcolm, M.A., & Moler, C.B. 1977, *Computer Methods for Mathematical Computations* (Englewood Cliffs, NJ: Prentice-Hall)
- Goodrich, R. W. & Miller, J. S. 1995, *ApJ*, 448, L73

- Gordon, K. D., Witt, A. N., Carruthers, G. R., Cristensen, S. A., & Dohne, B. C. 1994, *ApJ*, 432, 641
- Hansen, J.E., & Travis, L.D. 1974, *Space Science Reviews*, 16, 527
- Hester, J. J., et al. 1996, *AJ*, 1111, 2349
- Hines, D. C., Schmidt, G. D., Wills, B. J., Smith, P. S., & Sowinski, L. G. 1999, *ApJ*, 512, 145
- Hines, D. C., Wills, B. J. 1993, *ApJ*, 415, 82
- Hurt, T., Antonucci, R., Cohen, R., Kinney, A., & Krolik, J. 1999, *ApJ*, 514, 579
- Hovenier, J.W. 1971, *A&A*, 13, 7
- Jannuzi, B. T., Elston, R., Schmidt, G. D., Smith, P. S., & Stockman, H. S. 1995, *ApJ*, 454, L111
- Kartje, J.F. 1995, *ApJ*, 452, 565
- Kim, S. H., Martin, P. G. 1995, *ApJ*, 442, 172
- Laor, A., & Draine, B.T. 1993, *ApJ*, 402, 441
- Manzini, A., & di Serego Alighieri, S. 1996, *A&A*, 311, 79
- Mathis, J.S., Ruml, W., & Nordsieck, K.H. 1977, *ApJ*, 217, 425 (MRN)
- Miller, J. S., Goodrich, R. W., & Mathews, W. G. 1995, *ApJ*, 378, 47
- O'Dell, C. R., Wen, Z., & Hu, X. 1993, *ApJ*, 410, 696
- Rees, M. D., & Sitko, M. L. 1996, *ApJ*, 467, L105
- Sahai, R. et al. 1998a, *ApJ*, 492, L163
- Sahai, R. et al. 1998b, *ApJ*, 493, 301
- Schmidt, G. D., & Hines, D. C. 1999, *ApJ*, 512, 125
- Schulte-Ladbeck, R. E., et al. 1992, *ApJ*, 401, L105
- Tran, H. D. 1995a, *ApJ*, 440, 578
- Tran, H. D. 1995b, *ApJ*, 440, 597
- Tran, H. D., Cohen, M. H., Ogle, P. M., Goodrich, R. W., & di Serego Alighieri, S. 1998, *ApJ*, 500, 660
- Urry, C. M., & Padovani, P. 1995, *PASP*, 107, 803
- Van de Hulst, H.C. 1957, *Light Scattering by Small Particles* (New York: Wiley)
- White, R.L. 1979a, *ApJ*, 229, 954
- White, R.L. 1979b, *ApJ*, 230, 116
- Wills, B. J., et al. 1992, *ApJ*, 400, 96
- Wiscombe, W.J. 1976, *JQSRT*, 16, 637

- Wiscombe, W.J. 1979, Mie Scattering Calculations: Advances in Technique and Fast, Vector-Speed Computer Codes, NCAR/TN-140+STR (Boulder: National Center for Atmospherec Research) (a recently updated version of this report is available through Internet from the directory ftp://climate.gsfc.nasa.gov/pub/wiscomb/Single_Scatt/Mie_Code)
- Witt, A.N. 1977, ApJS, 35, 1
- Witt, A. N., Petersohn, J. K., Bohlin, R. C., O’Connell, R. W., Roberts, M. S., Smith, A. M., & Stecher, T. P. 1992, ApJ, 395, L5
- Witt, A. N., Petersohn, J. K., Holberg, J. B., Murthy, J., Dring, A., & Henry, R. C. 1993, ApJ, 410, 714
- Wolf, S., & Henning, Th. 1999, A&A, 341, 675
- Yanovitskij, E.G. 1997, Light Scattering in Inhomogeneous Atmospheres (Berlin: Springer)
- Zubko, V.G. 1999, in Physics and Chemistry of Interstellar Medium, ed. V. Ossenkopf (Aachen: Shaker Verlag), in press

A. Numerical implementation

A package of programs was developed to implement the calculations described above. The core of the package is the code PRT which calculates the polarized radiative transfer in a plane-parallel dusty slab using the adding-doubling method. The light scattering by an optically thick dusty sphere is calculated with the code PRT-SPH, using the results, obtained from PRT. The codes were all written in the standard ANSI C language, which allows a very efficient use of memory and CPU time. In particular, the memory for large multidimensional arrays, like the reflection and transmission matrices, which are a function of the number of Gaussian quadrature angles and the number of azimuth modes, is allocated dynamically (i.e. in run time). The codes may be ported to other computers where an ANSI C compiler is installed.

A.1. The code PRT

The development of PRT was simplified by the availability of the FORTRAN code RT3 generously provided by K.F. Evans and G.L. Stephens (Evans & Stephens 1991), which solves the polarized radiative transfer problem in the plane-parallel case. Some useful ideas and algorithms were adapted from RT3, although the realization of our code is completely different from that of RT3 both in the general structure and in the details of the code. RT3 was also very valuable for checking PRT during various steps of the its development.

The formulation of the problem that PRT solves is as follows. A plane-parallel slab is illuminated by unidirectional radiation from a point-like source and/or diffuse radiation from both above and/or below. The slab may be stratified, i.e. composed of a number of layers, each of which may be treated as homogeneous, having a specific geometrical thickness and dust grain composition. The dust in each layer may contain a number of size-distributed components, which may be spherical grains of various types: homogeneous, concentric multilayer and/or composite. The main task of PRT is to compute the angular-dependent intensity vectors (Stokes vectors) both for the radiation emergent from the upper and lower surface of the slab (external problem) and for the radiation at various levels inside the slab (internal problem). PRT solves this problem by the following algorithm:

1. reads input (see below), and allocates memory for arrays;
2. calculates quadrature angles and weights;
3. calculates the scattering matrix for each azimuth mode and each layer;
4. loop over the azimuth modes:
 - (a) loop over the layers:
 - i. initializes the doubling by calculating the local reflection and transmission matrices and source vectors for an initial very thin sublayer;
 - ii. doubling: computes the matrices and sources for the whole layer;
 - (b) adding: calculates the matrices and sources for the whole slab;
 - (c) calculates the intensity vectors, both external and internal;
5. converts the intensity vectors from Fourier modes into azimuth space;

6. calculates and outputs fluxes of emergent radiation;

The input includes one main file and a few additional smaller (one per layer) files. A typical main input file contains the following parameters: 1. the number of quadrature angles, n_μ , normally 16–24; 2. the number of azimuth modes, n_m , normally 4–24, but may be larger if the phase function is strongly forward peaked; 3. the number of Stokes parameters, n_{st} , 1–4; 4. quadrature scheme: Gaussian or double Gaussian; 5. the flux from the point source, F_0 , usually set to 1, and its zenith angle, θ_0 ; 6. the temperature of the diffuse radiation, incoming from above and below, usually set to 0 K; 7. the optical thickness of the initial doubling layer, τ_{in} , usually 10^{-6} – 10^{-5} ; 8. the wavelength, λ ; 9. the number of azimuths, n_ϕ , in the range 0° to 180° , for which output intensity vectors are to be calculated; 10. for each layer: its geometrical depth and the name of the additional input file with dust mixture properties.

A typical additional input file for a layer contains: 1. the dust mass density; 2. number of dust components; 3. for each dust component: type of grain constitution (homogeneous, multilayer, composite), mass fraction in per cent, name of a file with the size distribution function, the number of grain constituents (one for homogeneous grains), and for each grain constituent: name of the constituent and its volume fraction in the grain.

The output includes the angular-dependent intensities and fluxes of the radiation at various depths in the slab. In the simplest case, only the intensities at the top and bottom are printed (reflected and transmitted radiation). The results may be stored in text or in binary form. The binary form is especially suitable for use by other codes, e.g. when treating the light scattering by an optically thick sphere.

It is possible to use the Gaussian or the double Gaussian quadrature schemes in PRT. However, we have found that in order to produce results which are suitable for usage by PRT-SPH (for calculating light scattering by a sphere) the double Gaussian scheme is more preferable, as it generates an angle grid which contains very small μ , which is necessary for PRT-SPH to work properly.

The most important differences between the codes PRT and RT3 are as follow. (1) The memory for the multidimensional matrices and vectors in PRT is allocated and freed dynamically, which provides the most efficient scheme of memory usage, while in RT3 the arrays are statically allocated. (2) In PRT, the scattering matrix for a specified dust grain mixture is calculated using the Mie theory for individual grains summing over the mixtures components and grain-size distributions, whereas in RT3 the scattering matrix is computed from its expansion in Legendre series in $\cos \Theta_{scat}$. (3) PRT uses a more efficient realization of the FFT procedure with less than 50 lines of C code, whereas the respective FORTRAN code in the RT3 contains more than 250 lines. (4) When performing adding and doubling [eqs (47)] and calculating the intensities of the radiation inside the slab [eqs (49)], there is a need to work with inverted matrices. RT3 directly inverts matrices in these cases. In PRT, we proceed more efficiently. Since the inverted matrices in eqs (47) and (49) are combinations like $A^{-1}B$ or $A^{-1}b$ (where A and B are matrices, b is a vector), it is more computationally suitable to calculate $A^{-1}B$ or $A^{-1}b$ in the following way: first find the LU -decomposition of matrix A and then perform a backsubstitution with the columns of B or b (see e.g. Forsythe, Malcolm, & Moler 1977). This is more accurate and saves one matrix multiplication. (5) In addition to these differences, PRT was written with the aim of making it more readable and logically organized, and thus the general structure of PRT differs from RT3.

The improved computational scheme of PRT allows standard Mie theory solutions for grains with size parameters up to 10^6 . Thus, we do not need to resort to the Rayleigh-Gans or geometrical optics approximations (Bohren & Huffman 1983) for any combination of grain sizes and wavelengths.

The accuracy of the results generated by PRT depends on the following parameters: the initial optical thickness for doubling τ_{in} , the number of quadrature angles n_μ , and the number of azimuth modes n_m . For a proper choice of n_μ , usually ≥ 16 , and n_m , the accuracy is set by τ_{in} . For example, setting $\tau_{\text{in}} = 10^{-6}$ will result in 5–6 digit precision.

Typical values of running time and virtual memory, required by PRT for various values of n_μ and n_m are displayed in Table 1. These were derived by using a dusty layer of MRN dust. The results correspond to a calculation per one wavelength, $\lambda=0.5 \mu\text{m}$, and per one angle of incoming radiation, $\theta_0 = 30^\circ$. The optical depth of the layer at $\lambda=0.5 \mu\text{m}$ is ~ 224 ; τ_{in} for doubling was set to 10^{-6} . The calculations have been performed at a DEC Alpha workstation 250^{4/266}. The program was compiled with a C compiler GNU gcc.

A.2. The code PRT-SPH

The code PRT-SPH solves the following problem. A sphere of radius R_s is illuminated by unpolarized radiation with flux F_0 from a point source (see Figure 3), where the angle between the directions to the source and the observer is Θ_{obs} . The code PRT-SPH was designed to solve two main tasks: first, the computation of the linear and circular polarization maps that requires calculation of the local intensity vectors over the surface of the sphere, second, the calculation of the integrated characteristics: the intensity and the degree of linear polarization obtained by integrating the local intensities over the sphere. The local quantities are calculated using PRT.

The general algorithm that solves the problem is:

1. discretize the angles θ and Φ to define small local surface elements;
2. calculate local intensities and polarization parameters at each of the surface elements (eqs. 53–60 and 67–69);
3. calculate the total intensity vector and the degree of linear polarization (eqs. 62–65).

The azimuth angle Φ is discretized uniformly from -90° to 90° with n_Φ angles. The zenith angle grid is discretized with n_θ angles in the range $0-180^\circ$ such that all local elementary squares have equal surface area $\Delta S (= 2\pi R_s^2/n_\Phi n_\theta)$. The grid angles Φ_k and θ_k are defined by:

$$\Phi_k = 90^\circ \cdot \left[\frac{2}{n_\Phi} \left(k - \frac{1}{2} \right) - 1 \right], \quad k = 1, \dots, n_\Phi, \quad (\text{A1})$$

$$\cos \theta_k = 1 - \frac{2k-1}{n_\theta}, \quad k = 1, \dots, n_\theta. \quad (\text{A2})$$

The results of the computations for a slab obtained with PRT are output into a binary file, which contains the Fourier modes of the intensity vector of the reflected radiation $\vec{I}_t^{\uparrow m}$ for a number of fixed grid angles θ_{in} and θ_{out} . This provides the input to PRT-SPH. The local intensity vector \mathbf{I}_t^\uparrow [in eq. (57)] for any specific angles θ_{in} , θ_{out} and Φ_{out} is calculated as follows: first, by interpolating the Fourier modes for θ_{in} and θ_{out} , next by computing \mathbf{I}_t^\uparrow with formula (48) for the required Φ_{out} . For the two-dimensional interpolation over θ_{in} and θ_{out} , PRT-SPH uses bicubic splines. The accuracy of this approach for calculating \mathbf{I}_t^\uparrow generally lies well within 0.1% when a grid 16×16 for μ_{in} and μ_{out} is used for the PRT data.

To compute the integral parameters I_{sph} and Q_{sph} with formulae (62–63), the respective integrals are approximated by sums over the surface elements. For the grid of 40×90 for θ and Φ over the sphere, typical in our calculations, the accuracy of the results is better than 0.01–0.1%.

B. Code Testing

B.1. Comparison with analytic results for Rayleigh scattering

To test the accuracy of PRT and PRT-SPH, we performed calculations for a pure Rayleigh scattering sphere. This corresponds physically to a Thomson scattering electrons sphere. This case was carefully studied and there are various analytical results to compare with, e.g. Chandrasekhar (1960).

We calculated the inclination dependence of the intensity and the degree of linear polarization for radiation transmitted through an optically thick slab. We used $n_{\mu}=36$, $n_m=4$, $\tau_{\text{in}}=10^{-6}$ and $\tau=1460$ for the total optical depth of the scattering layer. The calculations made with PRT agree with the analytical results of Chandrasekhar (1960) to better than 0.05%.

The optical depth dependence of the flux of radiation transmitted through a Rayleigh scattering slab is shown in Figure 18, as calculated with PRT. For comparison, we plot the large- τ asymptotic analytic solution given by Yanovitskij (1997):

$$F_1(\tau) = \frac{4}{3} \frac{1.265}{\tau + 1.423} \quad (\text{B1})$$

We find an agreement to within 1% between the analytic and numerical solutions at $\tau > 3$.

As a side note, we tried to use our numerical solution, which is exact at all τ , to obtain an improved analytic approximation which generalizes equation B1 to a larger range of τ . We found a surprisingly good approximation to our result which is valid for *all* τ .

$$F_2(\tau) = \frac{4}{3} \frac{1.265 \cdot a}{\tau + 1.423 \cdot b} \quad (\text{B2})$$

with $a=1.019$ and $b=1.194$. The accuracy of this simple approximation is 0.3–2% for $\tau < 0.5$, 2–4% for $0.5 < \tau < 5$, and 0.5–2% for $5 < \tau$.

In a pure scattering atmosphere no flux is lost due to absorption, and thus energy conservation implies that the incident flux must equal the sum of transmitted and scattered fluxes. The right panel in Figure 18 shows the accuracy to which energy is conserved in PRT. There error increases roughly linearly with τ due to accumulation of errors in the doubling procedure. However, the errors for $\tau \sim 100 - 1000$, typical for this study, are still very small (< 0.0001 – 0.001%).

B.2. Comparison with previous results for a dusty sphere

White (1979b) calculated the scattering properties of an optically thick dusty sphere with an MRN composition, also using a doubling method for the radiative transfer. Figure 19 shows a comparison of the wavelength-dependent spherical albedo, maximum linear polarization, and ratio of forward to backward scattering, taken from the figures in White (1979b) to those calculated with PRT and PRT-SPH. The overall consistency is quite satisfactory, considering the significant improvements in the optical constants for graphite and silicate grains since the study of White (1979b).

C. Electron scattering versus dust scattering sphere

Figure 20 presents maps of the linear polarization of an optically thick electron scattering sphere, obtained with PRT-SPH. Comparison with corresponding maps of dusty spheres (Figs 13–15) indicates that, as expected, multiple scattering has a larger contribution to the polarization in the electron scattering sphere. For example, at $\Theta_{\text{obs}}=180^\circ$, the local degree of p reaches 7–8%, which is twice the value for a dusty sphere, and a similar effect is seen at very small Θ_{obs} . On the other hand, the maximum local polarization (at $\Theta_{\text{obs}}=90^\circ$), is 55–60% which is significantly lower than the maximum values of up to 90% (for $\lambda=0.05 \mu\text{m}$) found for a dusty sphere. Dust absorption enhances the polarization since it suppresses the contribution of multiple scattering, which adds unpolarized light, or light which is polarized at right angle to the single scattered light (for $\Theta_{\text{obs}}=90^\circ$), in both cases lowering the total polarization.

Figure 21 presents the integrated scattering characteristics of the electron scattering sphere in comparison to those of a dusty sphere. The electron scattering sphere scatters light more efficiently at most angles ($\Theta_{\text{obs}} > 20^\circ$). Its albedo is essentially unity, versus 4 – 11% only for a dusty sphere. However, a dusty sphere is a much more efficient polarizer, allowing maximum p_{sph} of 70–80%, versus only about 30% for the electron scattering sphere, again due to the greater contribution of multiple scattering in the later case.

Note that the integrated electron scattering sphere polarization is rotated by 90° for $\Theta_{\text{obs}}=0-20^\circ$. This effect is not seen in the Monte Carlo calculations of Code & Whitney (1995), most likely due to the very low intensity of light scattered at this range, coupled with the low polarization amplitude. This demonstrates the advantage of an accurate solution over Monte Carlo calculations, though the former is limited to the $\tau \gg 1$ case only.

Table 1. CPU time and virtual memory, required by PRT.

n_μ	n_m	CPU time	memory size
4	1	3 ^s 8	2.81 Mb
4	8	5 ^s 0	2.90 Mb
4	16	6 ^s 7	3.01 Mb
4	32	8 ^s 6	3.21 Mb
4	64	13 ^s 4	3.62 Mb
8	1	6 ^s 5	3.05 Mb
8	8	21 ^s 0	3.38 Mb
8	16	26 ^s 0	3.77 Mb
8	32	48 ^s 0	4.50 Mb
8	64	1 ^m 5	6.00 Mb
16	1	36 ^s 0	3.98 Mb
16	8	2 ^m 2	5.24 Mb
16	16	4 ^m 0	6.69 Mb
16	32	8 ^m 5	9.56 Mb
16	64	15 ^m 2	15.3 Mb
32	1	2 ^m 0	5.05 Mb
32	8	8 ^m 5	7.37 Mb
32	16	16 ^m 0	10.0 Mb
32	32	32 ^m 0	15.3 Mb
32	64	1 ^h 0	25.9 Mb

Fig. 1.— Schematic representation of light scattering by a slab of optical thickness τ_0 . Unpolarized radiation with a flux F_0 is incident from a zenith angle θ_0 . The downward and upward intensities (I^\downarrow and I^\uparrow) are a function of τ , $\mu = \cos \theta$ and azimuth angle Φ . Diffuse radiation may be incident from the top (I_t^\downarrow) and the bottom (I_b^\uparrow). The radiation which emerges from the top (I_t^\uparrow) and bottom (I_b^\downarrow), results from the transfer which is expressed by the reflection ($R^{\downarrow\uparrow}$, $R^{\uparrow\downarrow}$) and transmission ($T^{\downarrow\downarrow}$, $R^{\uparrow\uparrow}$) matrices, plus a possible contribution of internal sources (S^\downarrow , S^\uparrow).

Fig. 2.— The scattering geometry for a plane-parallel slab. The slab is in the XY plane and Z is the normal. The incoming beam makes an angle θ_{in} with the Z axis, and the outgoing beam is in the direction θ_{out} , Φ_{out} , where Φ_{out} is the azimuth difference between the incoming and outgoing beams. The scattering angle Θ_{scat} is the angle between the continuation of the incoming beam $A^{\text{in}}O$ and the outgoing beam OA^{out} . The rotations angles of the incoming (outgoing) beam i_1 (i_2) is measured from the meridian plane of the incoming beam $A^{\text{in}}OZ$ (the plane $A^{\text{out}}OZ$), specified by n_m^{in} (n_m^{out}), and the scattering plane $A^{\text{in}}OA^{\text{out}}$, specified by n_s^{in} (n_s^{out}). Right panel: A view of the scattering geometry along the outgoing beam, showing the plane of linear polarization of single scattered radiation, and of multiply scattered radiation. The first is generally at right angle to the plane defined by the incoming and outgoing beams, while the second is generally at right angle to the plane of the slab.

Fig. 3.— The scattering geometry for a dusty sphere. The direction of the incoming beam is $A^{\text{in}}S$, and it gets scattered by Θ_{obs} along the direction SA^{out} . The scattering point S coordinates on the sphere are zenith angle θ and azimuthal angle Φ (measured from the X axis), and the local normal is along $n(\theta, \Phi)$. The scattering at S is calculated using the local slab approximation, as presented in Figure 2.

Fig. 4.— The single scattering albedo and the phase function asymmetry parameter g as a function of wavelength. Note the sharp drop in albedo below 2200 Å, and the tendency of scattering to become strongly forward peaked at short wavelengths.

Fig. 5.— The extinction curve for the MRN dust mixture compared to the mean Galactic extinction curve for $R_V=3.1$ (Cardelli, Clayton, & Mathis 1989). Note that the Galactic extinction at 1000 Å is somewhat uncertain.

Fig. 6.— The scattering and polarization properties of optically thin MRN dust. Left panels show the λ dependence of the normalized intensity $I(\lambda, \Theta_{\text{scat}})/I(1 \mu\text{m}, 90^\circ)$, degree of linear polarization, $p(\lambda)$, and polarized intensity $I \times p$. Right panels show the Θ_{scat} dependence for the same parameters. The polarization plane is generally at right angle to the scattering plane, excluding the cases where $p(\lambda) < 0$ (marked by bold lines and filled points in the lower panels), which refer to polarization parallel to the scattering plane.

Fig. 7.— The logarithm of the total intensity $I_t(\lambda)$ of light scattered by an optically thick MRN dusty slab. Each row corresponds to a given μ_{in} , each column to a given Φ_{out} , and each subpanel presents curves for a range of μ_{out} . The incident flux is unity.

Fig. 8.— The degree of linear polarization for the same parameters as in Fig. 7.

Fig. 9.— The position angle of linear polarization for the same parameters as in Fig. 7.

Fig. 10.— The degree of circular polarization for the same parameters as in Fig. 7. Note that due to symmetry the circular polarization is zero at $\Phi_{\text{out}}=0^\circ$ and at 180° .

Fig. 11.— The linear polarization of the light backscattered (i.e. $\mu_{\text{in}} = \mu_{\text{out}}$, $\Phi_{\text{out}} = 180^\circ$) by an optically

thick slab as a function of λ and μ . Only multiple scatterings contribute to p in this case, and its amplitude is generally smaller by a factor of 10-20 compared with the single scattering contribution.

Fig. 12.— The plane albedo of an optically thick dusty MRN slab as a function of λ and μ_{in} . The albedo of an optically thick sphere is also indicated.

Fig. 13.— Maps of the linear and circular polarization of light scattered by an optically thick MRN dusty sphere at $\lambda = 0.05 \mu\text{m}$ for various Θ_{obs} . Note the very large differences in the relation between arrow size and polarization amplitude at different Θ_{obs} .

Fig. 14.— As in Figure 13 for $\lambda = 0.2124 \mu\text{m}$.

Fig. 15.— As in Figure 13 for $\lambda = 1.0 \mu\text{m}$.

Fig. 16.— The scattering and polarization properties of an optically thick MRN dusty sphere. All parameters are as shown in Fig. 6, excluding the intensity which is not normalized here.

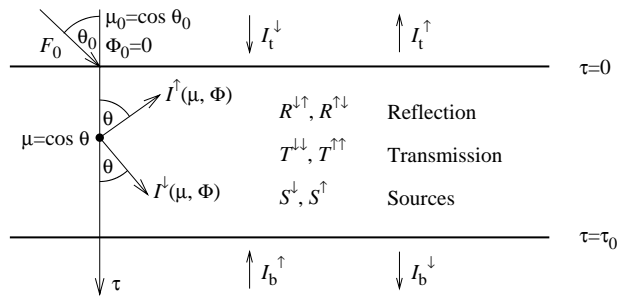
Fig. 17.— Comparison of scattering by optically thin dust versus an optically thick dusty sphere. Upper two panels show the λ dependence, and the lower two panels the Θ dependence. Note the large difference in the wavelength dependence of $I(\lambda, \Theta)/I(1 \mu\text{m}, \Theta)$ for the optically thin and thick cases, but the remarkable similarity of $p(\lambda)$.

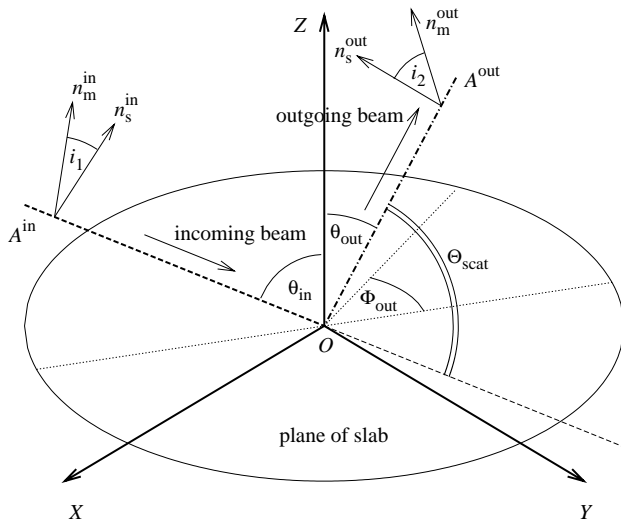
Fig. 18.— The flux of the radiation transmitted through a Rayleigh scattering slab as a function of optical thickness (*left panel*) as calculated with PRT. The incident flux is unity with $\mu_{\text{in}}=1$. The large- τ analytic asymptotic solution $F=\frac{4}{3}\frac{1.265}{\tau+1.423}$ of Yanovitskij (1997), agrees well with our results. We also show our improved approximation $F=\frac{4}{3}\frac{1.265\cdot a}{\tau+1.423\cdot b}$ with $a=1.019$ and $b=1.194$, which is accurate to 4.0% for all τ . The accumulated error in flux conservation, as calculated with PRT for the Rayleigh scattering atmosphere, is shown in the *right panel*.

Fig. 19.— Comparison with the earlier calculations of White (1979b) for the spherical albedo, maximum linear polarization, p_{max} , and ratio of forward to backward scattering, ρ , for scattering by an optically thick dusty sphere of the MRN dust composition. The agreement is acceptable, given the updates in the dielectric function since the study of White.

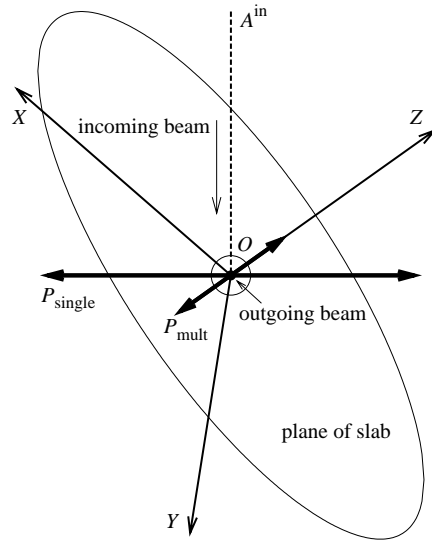
Fig. 20.— Maps of linear polarization of the light scattered by an optically thick Rayleigh scattering sphere (electron scattering) for various Θ_{obs} .

Fig. 21.— Comparison of the scattering properties of an optically thick electron scattering sphere versus an optically thick dusty sphere. The intensity of scattered light is generally much higher for an electron sphere, but its integrated polarization is significantly lower.





- incoming beam: $\mu_{in} = \cos \theta_{in}$
- - - - outgoing beam: $\mu_{out} = \cos \theta_{out}$, Φ_{out}
- projections of incoming and outgoing beams on XY plane



- A^{in} - - - - O scattering plane, seen edge-on
- $P_{single} \leftrightarrow$ polarization plane for single scattering
- $P_{mult} \leftrightarrow$ polarization plane for multiple scattering

